

# Robust Trajectory Tracking Control for Underactuated Autonomous Underwater Vehicles in Uncertain Environments

Shahab Heshmati-Alamdar<sup>ID</sup>, Alexandros Nikou, and Dimos V. Dimarogonas<sup>ID</sup>, *Senior Member, IEEE*

**Abstract**—This article addresses the tracking control problem of 3-D trajectories for underactuated underwater robotic vehicles operating in a constrained workspace including obstacles. More specifically, a robust nonlinear model predictive control (NMPC) scheme is presented for the case of underactuated autonomous underwater vehicles (AUVs) (i.e., unicycle-like vehicles actuated only in the surge, heave, and yaw). The purpose of the controller is to steer the unicycle-like AUV to the desired trajectory with guaranteed input and state constraints (e.g., obstacles, predefined vehicle velocity bounds, and thruster saturations) inside a partially known and dynamic environment where the knowledge of the operating workspace is constantly updated via the vehicle's onboard sensors. In particular, considering the sensing range of the vehicle, obstacle avoidance with any of the detected obstacles is guaranteed by the online generation of a collision-free trajectory tracking path, despite the model dynamic uncertainties and the presence of external disturbances representing ocean currents and waves. Finally, realistic simulation studies verify the performance and efficiency of the proposed framework.

**Note to Practitioners**—This article was motivated by the problem of robust trajectory tracking for an autonomous underwater vehicle (AUV) operating in an uncertain environment where the knowledge of the operating workspace (e.g., obstacle positions) is constantly updated online via the vehicle's onboard sensors (e.g., multibeam imaging sonars and laser-based vision systems). In addition, there may be other system limitations (e.g., thruster saturation limits) and other operational constraints, induced by the need of various common underwater tasks (e.g., a predefined vehicle speed limit for inspecting the seabed, and mosaicking), where it should also be considered into the control strategy. However, based on the existing trajectory tracking control approaches for underwater robotics, there is a lack of an autonomous control scheme that provides a complete and credible control strategy that takes the aforementioned issues into consideration. Based on this, we present a reliable control strategy that takes into account the aforementioned issues, along with dynamic uncertainties of the model and the presence of ocean currents. In future research, we will extend the proposed methodology for multiple

Manuscript received March 9, 2020; accepted April 30, 2020. This article was recommended for publication by Associate Editor C. K. Ahn and Editor K. Saitou upon evaluation of the reviewers' comments. This work was supported in part by the H2020 ERC Grant BUCOPHSYS, in part by the Swedish Foundation for Strategic Research (SSF), in part by the Swedish Research Council (VR), and in part by the Knut och Alice Wallenberg Foundation (KAW). (*Corresponding author:* Shahab Heshmati-Alamdar.)

Shahab Heshmati-Alamdar and Dimos V. Dimarogonas are with the Division of Decision and Control Systems, School of Electrical Engineering and Computer Science, KTH Royal Institute of Technology, 10044 Stockholm, Sweden (e-mail: shaha@kth.se; dimos@kth.se).

Alexandros Nikou is with Ericsson Research, 16440 Stockholm, Sweden (e-mail: alexandros.nikou@ericsson.com).

Color versions of one or more of the figures in this article are available online at <http://ieeexplore.ieee.org>.

Digital Object Identifier 10.1109/TASE.2020.3001183

AUV performing collaborative inspection tasks in an uncertain environment.

**Index Terms**—Marine navigation, predictive control, robust control, uncertain systems, unmanned autonomous vehicles, unmanned underwater vehicles.

## I. INTRODUCTION

DURING the last decades, considerable progress has been made in the field of unmanned marine vehicles, with a significant number of results in a variety of marine activities [1]. Applications such as ocean forecasting, deep-sea exploration, underwater inspection of oil/gas pipelines are indicative examples of applications that require the underwater robots to work under various constraints and increased levels of autonomy. In particular, autonomous underwater vehicles (AUVs) are characterized by constrained high-dimensional nonlinear dynamics, especially in the case of underactuated systems that induce significant complexity regarding model uncertainty as well as various operational constraints, such as sensing capabilities and visibility constraints [2].

A typical marine control problem is trajectory tracking [3]. Classical approaches such as local linearization and input-output decoupling have been used in the past to design motion controllers for underwater vehicles [4]. Nevertheless, the aforementioned methods yielded poor closed-loop performance, and the results were local, around only certain selected operating points. Output feedback linearization [5] is an alternative approach that, however, is not always possible. Moreover, based on a combined approach involving the Lyapunov theory and backstepping, various model-based nonlinear controllers have been proposed in the literature requiring very accurate knowledge of the vehicle dynamic parameters, which, in most cases, is quite difficult to obtain [6]. Moreover, the effect of ocean currents either is assumed to be known or an exponential observer is adopted for its estimation, thus increasing the design complexity [7].

Dynamic model uncertainties of AUVs have been mainly compensated by employing adaptive control techniques [8]. However, the application of these control strategies in a real-time experiment is questionable due to their sensitivity to unknown parameters. In addition, based on switching control strategies and backstepping techniques, a hybrid parameter adaptation law was presented in [9] and [10]. However, external disturbances and unmodeled dynamics were not considered. Moreover, sliding mode control, due to its strong

robustness against the uncertain model and time-varying parameters, is an alternative method that has been adopted in order to meet the problem of the dynamic model's uncertainties [11]–[13]. Nonetheless, the main disadvantage of the aforementioned control schemes is the inherent control input chattering that is energy intensive and may result in high-frequency dynamics, which is undesirable for underwater applications. Finally, adaptive neural network [11], [14], learning [15], [16], and fuzzy control [17], [18] schemes that deal with model uncertainties by exploiting the universal approximation capabilities of neural network and fuzzy system structures, but unfortunately, yield inevitably reduced levels of robustness against modeling imperfections [19].

In addition, by employing all of the aforementioned motion control strategies, it is not always feasible or straightforward to incorporate input (generalized body forces/torques or thrust) and state (3-D obstacles and velocities) constraints into the vehicle's closed-loop motion [20]. In that sense, the trajectory control problem of underwater robots continues to pose considerable challenges to system designers, especially in view of the high-demanding missions envisioned by the marine industry (e.g., surveillance of oil platforms and cable tracking). In this context, nonlinear model predictive control (NMPC) [21] can be considered a suitable approach for complex underwater missions, as it is able to handle efficiently input and state constraints, while dealing with parameter uncertainties through its robustness [22]. A sampling-based model predictive control scheme was proposed in [23] for motion control of underwater vehicles in the presence of constraints. A depth control strategy for an overactuated AUV based on linear model predictive control was presented in [24]. However, actuator limits were the only considered constraints of the system. In [25], an MPC framework was proposed for the trajectory tracking of a full-actuated AUV under state constraints without taking into account the effects of disturbances and model uncertainties. In the aforementioned studies, the validation of the proposed strategies was conducted via simple simulation tests. Experimental validation of an NMPC scheme for robust stabilization of an AUV was presented in [20].

The reference trajectory for the underwater robot is usually the result of some path planning techniques [26]. The majority of planning techniques are based on offline optimization schemes that consider static or quasi-static operational environments. Their output is often a set of waypoints or trajectories satisfying certain environmental constraints (i.e., known obstacles). On the other hand, robust AUV control around coral reefs is difficult because of their unstructured dynamic nature. In the absence of GPS in the underwater environment, localization errors are increasing, making any prior knowledge of the environment coarse and inappropriate. Nonetheless, the reference trajectory might not be feasible in real ocean environments due to the fact that the ocean is a partially known environment even in the best case scenario. When operating in such an uncertain environment, the underwater vehicle has to be reactive and has the ability to recalculate its path online in order to generate collision-free paths, as more information about the surroundings becomes available [27].

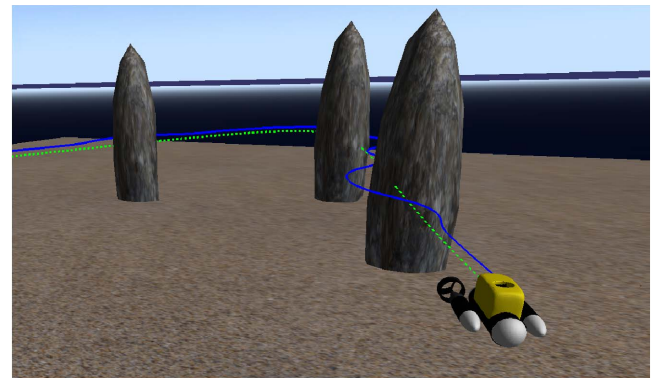


Fig. 1. Trajectory tracking in the uncertain and constrained workspace, including obstacles where the knowledge of the operating workspace (e.g., the accurate obstacles' positions) is constantly updated via the vehicle's onboard sensors. The reference and actual vehicle trajectories are depicted with green dashed and blue lines, respectively.

Motivated by the aforementioned considerations, this article presents a robust trajectory tracking control scheme for underactuated AUVs operating in a constrained workspace, including obstacles (see Fig. 1). In particular, a robust NMPC scheme is presented for the underactuated AUVs (i.e., vehicles actuated only in the surge, heave, and yaw). Various constraints such as sparse obstacles, workspace boundaries, sensing range capability, predefined upper bounds for the velocity of the underwater robotic vehicle (requirements for several underwater tasks, such as seabed inspection scenario and mosaicking), and thruster saturation are considered during the control design. The purpose of the controller is to steer the underactuated AUV on a desired trajectory inside a constrained and dynamic workspace. Since the knowledge of the operating workspace is constantly updated online via the vehicle's onboard sensors, the robot recalculates its path online and generates a collision-free trajectory tracking path if the updated environmental changes (i.e., new detected obstacles) are in conflict with the reference trajectory. In particular, by considering a ball that covers the volume of the system and the sensing range of the vehicle, obstacle avoidance with any of the detected obstacles is guaranteed by the online generation of a collision-free trajectory tracking path, despite the model dynamic uncertainties and the presence of external disturbances representing ocean currents and waves. The proposed feedback control law consists of two parts: an online law that is the outcome of a finite horizon optimal control problem (FHOCP) solved for the nominal dynamics, and a state feedback law that is tuned offline and guarantees that the real trajectories remain bounded in a tube centered along the nominal trajectories for all times. The volume of the tube depends on the upper bound of the disturbances as well as bounds of derivatives of the dynamics. The closed-loop system has analytically guaranteed stability and convergence properties.

The rest of this article is organized as follows. Section II provides the notation and the mathematical preliminaries. The problem treated in this article in hand is formulated in Section III. Section IV analyzes the proposed framework.

In Section V, a simulation study is demonstrated through figures and a video. Finally, in Section VI, conclusions and future research directions are discussed.

## II. NOTATION AND BACKGROUND

The sets of positive integers and real numbers are denoted by  $\mathbb{N}$  and  $\mathbb{R}$ , respectively.  $\mathbb{R}_{\geq 0}^n$  and  $\mathbb{R}_{>0}^n$  are the sets of real  $n$  vectors with all elements nonnegative and positive, respectively. Given a set  $\mathcal{S}$ , denote by  $|\mathcal{S}|$  and  $\mathcal{S}^n := \mathcal{S} \times \dots \times \mathcal{S}$  its cardinality and its  $n$ -fold Cartesian product. Given a vector  $z \in \mathbb{R}^n$ , define by  $\|z\|_2 := (z^\top z)^{1/2}$ ,  $\|z\|_\infty := \max_{i=1,\dots,n} |z_i|$ , and  $\|z\|_P := (z^\top P z)^{1/2}$  its Euclidean, infinite, and  $P$ -weighted norm, respectively, with  $P \geq 0$ . The notation  $\lambda_{\min}(P)$  stands for the minimum absolute value of the real part of the eigenvalues of  $P \in \mathbb{R}^{n \times n}$ ;  $0_{m \times n} \in \mathbb{R}^{m \times n}$  and  $I_n \in \mathbb{R}^{n \times n}$  stand for the  $m \times n$  matrix with all entries zeros and the identity matrix, respectively. The notation  $\text{diag}\{P_1, \dots, P_n\}$  stands for the block diagonal matrix with the matrices  $P_1, \dots, P_n$  in the main diagonal. Moreover,  $\mathcal{B}(\mathbf{c}, r) := \{\mathbf{x} \in \mathbb{R}^n : \|\mathbf{x} - \mathbf{c}\|_2 \leq r\}$  stands for a ball in  $\mathbb{R}^n$  with center and radius  $\mathbf{c} \in \mathbb{R}^n$ ,  $r > 0$ , respectively. The boundary of a set  $A$  is denoted as  $\partial A$  and is defined as  $\partial A = A \setminus \mathring{A}$ , where  $\mathring{A}$  is the interior of set  $A$ . Given sets  $\mathcal{S}_1, \mathcal{Z} \subseteq \mathbb{R}^n$ , and  $\mathcal{S}_2 \subseteq \mathbb{R}^m$  and matrix  $P \in \mathbb{R}^{n \times m}$ , the Minkowski addition, the Pontryagin difference, and the matrix-set multiplication are defined by  $\mathcal{S}_1 \oplus \mathcal{Z} := \{s_1 + z : s_1 \in \mathcal{S}_1, z \in \mathcal{Z}\}$ ,  $\mathcal{S}_1 \ominus \mathcal{Z} := \{s_1 \in \mathcal{S}_1 : s_1 + z \in \mathcal{S}_1, \forall z \in \mathcal{Z}\}$ , and  $P \circ \mathcal{S}_2 := \{Ps : s \in \mathcal{S}_2\}$ , respectively.

*Definition 1* ([28]): Consider a dynamical system

$$\dot{\mathbf{x}} = f(\mathbf{x}, \mathbf{u}, \mathbf{d}), \quad \mathbf{x} \in \mathcal{X}, \quad \mathbf{u} \in \mathcal{U}, \quad \mathbf{d} \in \mathcal{D}$$

with initial condition  $\mathbf{x}(0) \in \mathcal{X}$  and external disturbances  $\mathbf{d} \in \mathcal{D}$ . A set  $\mathcal{X}' \subseteq \mathcal{X}$  is a robust control invariant (RCI) set for the system if there exists a feedback control law  $\mathbf{u} := \kappa(\mathbf{x}) \in \mathcal{U}$  such that for all  $\mathbf{x}(0) \in \mathcal{X}'$  and for all  $\mathbf{d} \in \mathcal{D}$ , it holds that  $\mathbf{x}(t) \in \mathcal{X}'$  for all  $t \geq 0$ , along every solution  $\mathbf{x}(t)$  of the closed-loop system.

*Definition 2*: A nonlinear system  $\dot{\mathbf{x}} = f(\mathbf{x}, \mathbf{u}, \mathbf{d})$ ,  $\mathbf{x} \in \mathcal{X}$ ,  $\mathbf{u} \in \mathcal{U}$ ,  $\mathbf{d} \in \mathcal{D}$ , with initial condition  $\mathbf{x}(0) \in \mathcal{X}$ , is said to be input-to-state stable (ISS) with respect to  $\mathbf{d} \in \mathcal{D}$  if there exist functions  $\beta \in \mathcal{KL}$  and  $\gamma \in \mathcal{K}$  such that for any initial condition  $\mathbf{x}(0) \in \mathcal{X}$  and for any input  $\mathbf{u}(t) \in \mathcal{U}$ , the solution  $\mathbf{x}(t)$  exists for all  $t \in \mathbb{R}_{\geq 0}$  and satisfies

$$\|\mathbf{x}(t)\| \leq \beta(\|\mathbf{x}(0)\|, t) + \gamma \left( \sup_{0 \leq s \leq t} \|\mathbf{d}(s)\| \right).$$

## III. PROBLEM STATEMENT

In this section, the overall problem is formulated. Initially, the mathematical model of the underactuated underwater vehicle is presented.

### A. Mathematical Modeling

The pose vector of the vehicle with respect to the inertial frame  $\mathcal{I}$  is denoted by  $\eta_{\text{tot}} = [\eta_1^\top \eta_2^\top]^\top \in \mathbb{R}^6$ , including the position (i.e.,  $\eta_1 = [x \ y \ z]^\top$ ) and orientation (i.e.,  $\eta_2 = [\phi \ \theta \ \psi]^\top$ ) vectors. The  $\mathbf{v}_{\text{tot}} = [\mathbf{v}_1^\top \ \mathbf{v}_2^\top]^\top \in \mathbb{R}^6$  is

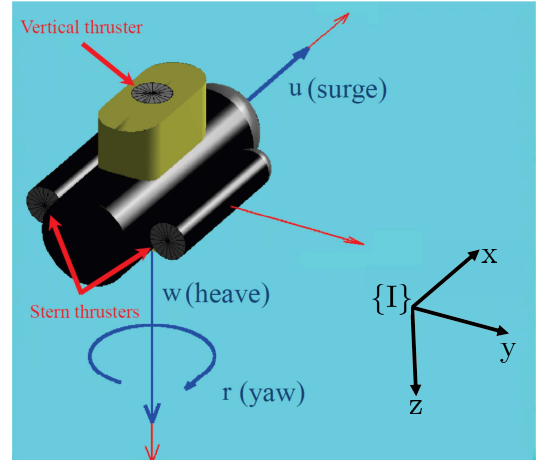


Fig. 2. Underactuated unicycle-like underwater vehicle. Blue color indicates the actuated degrees of freedom.

the velocity vector of the vehicle expressed in body fixed frame  $\mathcal{V}$  and includes the linear (i.e.,  $\mathbf{v}_1 = [u \ v \ w]^\top$ ) and angular (i.e.,  $\mathbf{v}_2 = [p \ q \ r]^\top$ ) velocity vectors (see Fig. 2). In this work, we consider one of the most common types of underactuated underwater vehicles, namely unicycle-like vehicles (see Fig. 2). The considered unicycle-like vehicles are equipped with a set of thrusters that are effective only in surge, heave, and yaw motion (see Fig. 2), meaning that the vehicle is underactuated along the sway axis.

*Remark 1*: The unicycle-like underactuated underwater vehicles considered in this work are usually designed with metacentric restoring forces in order to regulate roll and pitch angles. Thus, the angles  $\phi$  and  $\theta$  and angular velocities  $p$  and  $q$  are negligible, and we can consider them to be equal to zero [29]. In addition, the vehicle is symmetric about the  $xz$  plane and close to symmetric about the  $yz$  plane. Therefore, we can safely assume that motions in heave, roll, and pitch are decoupled [30].

Without loss of generality and based on the aforementioned considerations, the dynamic equations of the considered underwater robotic vehicle can be given as follows [30]:

$$\dot{x} = u \cos \psi - v \sin \psi \quad (1a)$$

$$\dot{y} = u \sin \psi + v \cos \psi \quad (1b)$$

$$\dot{z} = w \quad (1c)$$

$$\dot{\psi} = r \quad (1d)$$

$$\dot{u} = \frac{1}{m_{11}} [m_{22}vr + X_u u + X_{u|u}|u|u + \tau_X] \quad (1e)$$

$$\dot{v} = \frac{1}{m_{22}} [-m_{11}ur + Y_v v + Y_{v|v}|v|v] \quad (1f)$$

$$\dot{w} = \frac{1}{m_{33}} [(W - B) + Z_w w + Z_{w|w}|w|w + \tau_Z] \quad (1g)$$

$$\dot{r} = \frac{1}{m_{44}} [(m_{11} - m_{22})uv + N_r r + N_{r|r}|r|r + \tau_N] \quad (1h)$$

where  $m_{11}$ ,  $m_{22}$ ,  $m_{33}$ , and  $m_{44}$  are the terms of the inertia matrix, including the added mass,  $W$  and  $B$  are the vehicle weight and the buoyancy force,  $X_u$ ,  $X_{u|u}$ ,  $Y_v$ ,  $Y_{v|v}$ ,  $Z_w$ ,  $Z_{w|w}$ ,  $N_r$ , and  $N_{r|r}$  are negative hydrodynamic damping coefficients, and  $\tau_X$ ,  $\tau_Z$ , and  $\tau_N$  are the control inputs of the system and

consist of body forces and torque generated by the thrusters along the surge, heave, and yaw directions.

*Remark 2:* In this work, we consider one of the most common types of underactuated underwater vehicles, namely the unicycle-like vehicles (see Fig. 2). In particular, the unicycle-like underactuated vehicles considered in this class are actuated by forces  $\tau_x$  and  $\tau_z$  along the longitudinal (surge) and vertical (heave) axes, respectively, and a torque  $\tau_y$  about the vertical (yaw) axis (see Fig. 2). The aforementioned forces  $\tau_x$  and  $\tau_z$  and torque  $\tau_y$  define the input control variables of the corresponding dynamic system (1), which, in this case, is unactuated in the sway degree of freedom (i.e.,  $\tau_y = 0$ ).

The dynamic equations of (1) can be rewritten as

$$\dot{\eta} = J(\eta)v + g(\eta, v) \quad (2a)$$

$$\dot{v} = M^{-1}[\tau + C(v, v)v + D(v)v + g] \quad (2b)$$

$$\dot{v} = \frac{1}{m_{22}}[-m_{11}ur + Y_v v + Y_{v|v|}|v|v] \quad (2c)$$

where the following holds.

- 1)  $\eta = [x \ y \ z \ \psi]^T \in \mathbb{R}^4$  is the pose vector expressed in  $\mathcal{I}$ .
- 2)  $v = [u, \ w, \ r]^T \in \mathbb{R}^3$  is the velocity vector of the vehicle along actuated degrees of freedom, expressed in the body-fixed frame  $\mathcal{V}$ .
- 3)  $\tau = [\tau_x, \ \tau_z, \ \tau_y]^T \in \mathbb{R}^3$  is the propulsion force/torque vector (i.e., the body forces and torques generated by the thrusters) applied on the vehicle and expressed in body-fixed frame  $\mathcal{V}$ .
- 4)  $g(\eta, v) = [-s_\psi, \ c_\psi, \ 0, \ 0]^T v$ .
- 5)  $M = \text{diag}(m_{11}, m_{33}, m_{44}) \in \mathbb{R}^{3 \times 3}$  is the inertia matrix.
- 6)

$$C(v, v) = \begin{bmatrix} 0 & 0 & m_{22}v \\ 0 & 0 & 0 \\ (m_{11} - m_{22})v & 0 & 0 \end{bmatrix}$$

is the coriolis matrix.

7)

$$D(v) = \begin{bmatrix} X_u + X_{u|u|}|u| & 0 & 0 \\ 0 & Z_w + Z_{w|w|}|w| & 0 \\ 0 & 0 & N_r + N_{r|r|}|r| \end{bmatrix}$$

is the drag matrix.

- 8)  $g = [0, (W - B), 0]^T \in \mathbb{R}^3$  is the hydrostatic restoring force vector.

9)

$$J(\eta) = \begin{bmatrix} \cos(\psi) & 0 & 0 \\ \sin(\psi) & 0 & 0 \\ 0 & 1 & 0 \\ 0 & 0 & 1 \end{bmatrix} \in \mathbb{R}^{4 \times 3}$$

is the Jacobian matrix transforming the velocities from the body-fixed ( $\mathcal{V}$ ) to the inertial ( $\mathcal{I}$ ) frame.

Notice that the robot moves under the influence of an irrotational current that behaves as an external disturbance on the system's dynamic equation (2b). In particular, we set  $\delta_y$  and  $\delta = [\delta_x, \delta_z, \delta_y]^T \in \Delta \subset \mathbb{R}^3$  with  $\Delta$  being a compact set. In this vein, there exist upper bounds  $\bar{\delta}_y > 0$  and  $\bar{\delta} > 0$  such that  $|\delta_y| \leq \bar{\delta}_y$  and  $||\delta|| \leq \bar{\delta}$ , respectively. Furthermore,

it is assumed that vehicle's dynamic parameters have been identified via a proper identification scheme. However, some degree of model uncertainty should be considered. In particular, we set  $\gamma_Y$  as the model uncertainty regarding the sway direction and  $\gamma = [\gamma_x, \gamma_z, \gamma_N]^T \in \Gamma \subset \mathbb{R}^3$  as the vector of uncertainties with  $\Gamma$  being a compact set. In the same vein, we assume that there exist positive upper bounds  $\bar{\gamma}_Y$  and  $\bar{\gamma} \geq 0$  such that  $|\gamma_Y| \leq \bar{\gamma}_Y$  and  $||\gamma|| \leq \bar{\gamma}$ . Taking into consideration the aforementioned disturbances and uncertainties, we can model the perturbed system as follows:

$$\dot{\eta} = J(\eta)v + g(\eta, v) \quad (3a)$$

$$\dot{v} = M^{-1}[\tau + C(v, v)v + D(v)v + g] + \xi \quad (3b)$$

$$\dot{v} = \frac{1}{m_{22}}[-m_{11}ur + Y_v v + Y_{v|v|}|v|v] + \delta_Y \quad (3c)$$

where  $\xi = \gamma + \delta \in \Xi \subset \mathbb{R}^3$  in the vector that is the result of adding uncertainties and external disturbances and  $\Xi$  is a compact set with  $\Xi = \Delta \oplus \Gamma$ . Since the sets  $\Delta$  and  $\Gamma$  are compact, we have that  $\Xi$  is also compact, and

$$\Xi := \{\xi(t) \in \mathbb{R}^3 : ||\xi(t)||_2 \leq \bar{\xi}\} \quad (4)$$

with  $\bar{\xi} \triangleq \bar{\delta} + \bar{\gamma}$ .

### B. Geometry of the Workspace

We consider that the underwater vehicle operates inside a workspace  $\mathcal{W} \subset \mathbb{R}^3$  with boundary  $\partial\mathcal{W}$  and scattered obstacles located within it. Without loss of the generality, the robot and the obstacles are modeled by spheres (i.e., we adopt the spherical world representation [31]). Let  $\mathcal{B}(\eta_1, \tilde{r})$  be a closed ball that covers the whole vehicle volume (main body and additional equipments). Moreover, let  $\mathcal{B}(\eta_1, \bar{R})$  with  $\bar{R} > \tilde{r}$  be a sensing area where the robot can perceive and update its knowledge of the workspace (i.e., the obstacle locations) using its onboard sensors. Furthermore, the  $\mathcal{M}$  static obstacles within the workspace are defined as closed balls described by  $\pi_m = \mathcal{B}(p_{\pi_m}, r_{\pi_m})$ ,  $m \in \{1, \dots, \mathcal{M}\}$ , where  $p_{\pi_m} \in \mathbb{R}^3$  is the center and  $r_{\pi_m} > 0$  is the radius of the obstacle  $\pi_m$ . In addition, based on the property of spherical world [31], for each pair of obstacles  $m, m'$  with  $m \neq m'$ , we have  $||\pi_m - \pi_{m'}|| > 2\tilde{r} + r_{\pi_m} + r_{\pi'_{m'}}$ , which intuitively means that the obstacles  $m$  and  $m'$  are disjoint in such a way that the entire volume of the vehicle can pass through the free space between them. Therefore, there exists a feasible trajectory  $\eta_1(t)$  for the vehicle such that

$$\mathcal{B}(\eta_1(t), \tilde{r}) \cap \{\mathcal{B}(p_{\pi_m}, r_{\pi_m}) \cup \partial\mathcal{W}\} = \emptyset \quad \forall t \geq 0, \quad m \in \{1, \dots, \mathcal{M}\}. \quad (5)$$

A graphical representation of the feasible trajectory is depicted in Fig. 3.

### C. Constraints

1) *State Constraints:* As already stated, the robot should be able to avoid the newly detected obstacles that may have been unknown to the off-line trajectory planner. Moreover, for the needs of several common underwater tasks (e.g., seabed inspection and mosaicking), the vehicle is required to move

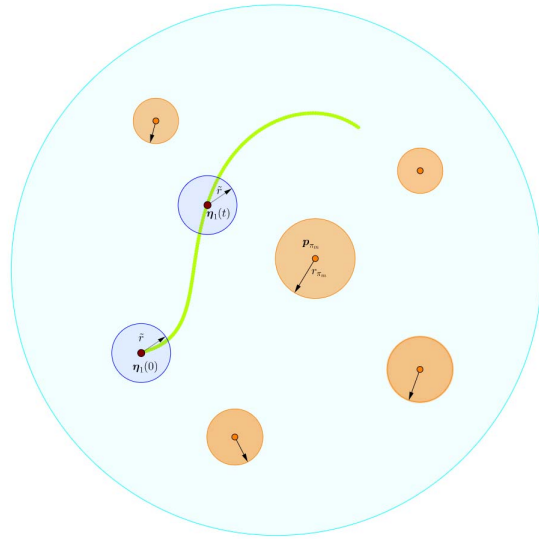


Fig. 3. Graphical representation of a feasible trajectory in the workspace. The boundary of workspace  $\partial\mathcal{W}$  is illustrated in cyan. The orange areas indicate the obstacles within the workspace  $\mathcal{W}$ . The blue line encircles the area covered by the vehicle at times 0 and  $t$  with  $t > 0$ , respectively. The feasible trajectory of the vehicle is depicted in green.

with relatively low speeds with upper bound denoted by  $\bar{v}$  and the velocity vector  $\bar{v} = [\bar{u} \ \bar{w} \ \bar{r}]^\top$ , where  $(\cdot)$  denotes the corresponding upper bounds for each coefficient. These requirements are captured by the state constraint sets  $H$  and  $V$ , given by

$$\eta(t) \in H \subset \mathbb{R}^4, \quad \text{and} \quad v(t) \in V \subset \mathbb{R}^3 \quad (6)$$

which can be defined as

$$V := \{v \in \mathbb{R}^3 : |u| \leq \bar{u}, |w| \leq \bar{w}, |r| \leq \bar{r}\} \quad (7)$$

with upper bound as  $\bar{V} = (\bar{u} + \bar{w} + \bar{r})^{(1/2)}$ , and

$$H := \{\eta \in \mathbb{R}^4 : \mathcal{B}(\eta_1, \tilde{r}) \cap \{\mathcal{B}(p_{\pi_m}, r_{\pi_m}) \cup \partial\mathcal{W}\} = \emptyset \quad m \in \{1, \dots, M\}\}. \quad (8)$$

2) *Input Constraints:* The actuation body forces and torques are generated by the thrusters. Thus, we define the control constraint set  $T$  as follows:

$$\tau(t) = [\tau_X, \ \tau_Z, \ \tau_N]^\top \in T \subseteq \mathbb{R}^3 \quad (9)$$

which can be defined as

$$T := \{\tau \in \mathbb{R}^3 : |\tau_X| \leq \bar{\tau}_X, |\tau_Z| \leq \bar{\tau}_Z, |\tau_N| \leq \bar{\tau}_N\} \quad (10)$$

with  $\bar{\tau}_X, \bar{\tau}_Z, \bar{\tau}_N \in \mathbb{R}_{\geq 0}$  are the corresponding upper bound for each thrust directions.

#### D. Problem Statement

Let  $p_d(t) = [x_d(t), y_d(t), z_d(t)]^\top$  denote a smooth desired trajectory with bounded time derivatives; thus, the problem of this article can be stated as follows.

*Problem 1 (Robust Tracking Control for an Autonomous Underactuated Underwater Vehicle):* Consider an underactuated AUV described by (3) operating in a workspace  $\mathcal{W} \subset$

$\mathbb{R}^3$  with state and input constraints as well as disturbances imposed by the sets  $H$ ,  $V$ , and  $T$  as well as  $\Xi$  as in (6), (9) and (4), respectively. Consider also that the robot and the obstacles are all modeled according to the spherical world representation,<sup>1</sup> and the knowledge of the operating workspace  $\mathcal{W}$  (e.g., obstacles positions) is constantly updated via the vehicle's onboard sensors inside a sensing region defined by  $\mathcal{B}(\eta_1, \bar{R})$ . Given a desired trajectory  $p_d(t) = [x_d(t), y_d(t), z_d(t)]^\top$ , design a feedback control law  $\tau = \kappa(\eta, v) \in T$  such that the desired trajectory  $p_d(t)$  is tracked while guaranteeing the following specifications:

- 1) capability to be flexible regarding environmental changes (i.e., avoiding new detected obstacles which may coincide with desired trajectory, and so on);
  - 2) respect operational limitations in the form of state (e.g., velocity bounds) and input (thrust saturation) constraints
- $$\eta(t) \in H, \quad v(t) \in V, \quad \tau(t) \in T$$
- 3) respect capability sensing range of the system;
  - 4) predefined robustness with respect to the external disturbances and model uncertainties.

#### IV. METHODOLOGY

In this section, we present, in detail, the methodology proposed in order to formulate the solution of Problem 1. In particular, an NMPC framework [32]–[35] is utilized, and a relevant robust NMPC analysis, the so-called tube-based approach, is provided here for the trajectory tracking problem for underactuated systems in the presence of disturbances. The proposed feedback control law consists of two parts: an online control law, which is the outcome of FHOCP for the nominal system dynamics, and a state feedback law, which guarantees that the real system trajectories always lie within a tube centered along the nominal trajectories. First, we begin by defining the error states and the corresponding transformed constraints.

##### A. Error Definitions

Given the desired trajectory  $p_d(t) = [x_d(t), y_d(t), z_d(t)]^\top$ , let us define the position errors

$$e_x(t) = x - x_d(t), \quad e_y(t) = y - y_d(t), \quad e_z(t) = z - z_d(t) \quad (11)$$

the projected on the horizontal plane distance error

$$e_d(t) = \sqrt{e_x^2(t) + e_y^2(t)} \quad (12)$$

as well as the projected on the horizontal plane orientation error

$$e_o(t) = \frac{e_y(t)}{e_d(t)} c_{\psi(t)} - \frac{e_x(t)}{e_d(t)} s_{\psi(t)} = s_{\psi_e} \quad (13)$$

where  $s_* = \sin(\star)$ ,  $c_* = \cos(\star)$ ,  $\psi$  is the yaw angle, and  $\psi_e$  is the angle measured from the normalized error vector

$$\mathbf{e}_d = \left[ \frac{e_x}{e_d}, \frac{e_y}{e_d}, 0 \right]^\top$$

<sup>1</sup>As described in Section III-B.

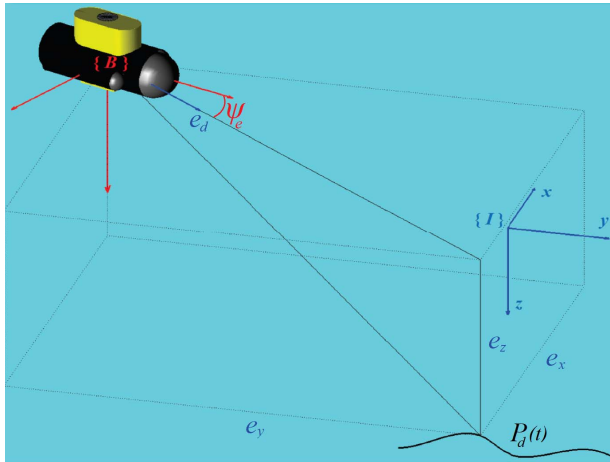


Fig. 4. Graphical illustration of the error definition.

on the horizontal plane to the normalized projection of the longitudinal axis of the vehicle on the horizontal plane, defined by the vector  $[c_\psi, s_\psi, 0]^\top$  (see Fig. 4). Now, differentiating the aforementioned errors of (11)–(13), employing (2), and using the

$$\begin{aligned} c_{\psi_e} &= \frac{e_x}{e_d} c_\psi + \frac{e_y}{e_d} s_\psi \\ c_{\psi+\psi_e} &= c_\psi c_{\psi_e} - s_\psi s_{\psi_e} = \frac{e_x}{e_d} \\ s_{\psi+\psi_e} &= s_\psi c_{\psi_e} + c_\psi s_{\psi_e} = \frac{e_y}{e_d} \end{aligned}$$

we arrive at

$$\dot{e}_d = c_{\psi_e} u - \dot{x}_d c_{\psi+\psi_e} - \dot{y}_d s_{\psi+\psi_e} + s_{\psi_e} v \quad (14)$$

$$\dot{e}_z = \dot{z} - \dot{z}_d \Rightarrow \dot{e}_z = w - \dot{z}_d \quad (15)$$

$$\begin{aligned} \dot{e}_o &= -\frac{s_{\psi_e} c_{\psi_e}}{e_d} u - c_{\psi_e} r + \frac{\dot{x}_d}{e_d} [s_{\psi_e} c_{\psi+\psi_e} + s_\psi] \\ &\quad + \frac{\dot{y}_d}{e_d} [s_{\psi_e} s_{\psi+\psi_e} - c_\psi] + \frac{c_{\psi_e}^2}{e_d} v. \end{aligned} \quad (16)$$

By defining the error vector  $\mathbf{e} = [e_d, e_z, e_o]^\top$ , the aforementioned formulas can be written in matrix form as

$$\dot{\mathbf{e}} = J(\mathbf{e}, \mathbf{p}_d) \mathbf{v} + \zeta(\mathbf{e}, \dot{\mathbf{p}}_d) + \xi(\mathbf{e}, v) \quad (17)$$

where

$$\begin{aligned} J(\mathbf{e}, \mathbf{p}_d) &:= \begin{bmatrix} c_{\psi_e} & 0 & 0 \\ 0 & 1 & 0 \\ -\frac{s_{\psi_e} c_{\psi_e}}{e_d} & 0 & -c_{\psi_e} \end{bmatrix}, \quad \xi(\mathbf{e}, v) := \begin{bmatrix} s_{\psi_e} v \\ 0 \\ \frac{c_{\psi_e}^2}{e_d} v \end{bmatrix} \\ \zeta(\mathbf{e}, \dot{\mathbf{p}}_d) &:= \begin{bmatrix} -\dot{x}_d c_{\psi-\psi_e} - \dot{y}_d s_{\psi-\psi_e} \\ -\dot{z}_d \\ \dot{x}_d [s_{\psi_e} c_{\psi+\psi_e} + s_\psi] + \frac{\dot{y}_d}{e_d} [s_{\psi_e} s_{\psi+\psi_e} - c_\psi] \end{bmatrix} \end{aligned}$$

which are the transformed kinematic error equations of the underwater vehicle system. It should be noted that the tracking control problem is solved if the projected on the horizontal plane distance error  $e_d$ , the vertical error  $e_z$ , and the orientation error  $e_o$  converge to zero. Moreover, it should be noticed that

the orientation error  $e_o$  as well as the Jacobian matrix  $J(\mathbf{e}, \mathbf{p}_d)$  are well-defined when the following holds:

$$e_d(t) > 0 \text{ and } -\frac{\pi}{2} < \psi_e < \frac{\pi}{2} \quad \forall t \geq 0. \quad (18)$$

Thus, a feasible error configuration imposed to the system is captured by the set

$$\mathcal{E} := \left\{ \eta \in H : \sqrt{e_x^2 + e_y^2} \geq \epsilon_d, -\frac{\pi}{2} + \epsilon_r \leq \psi_e \leq \frac{\pi}{2} - \epsilon_r \right\} \quad (19)$$

where  $\epsilon_d$  and  $\epsilon_r$  are arbitrarily small positive constants that guarantee avoidance of the aforementioned singularity issues.

*Remark 3:* It should be noted that in  $J(\mathbf{e}, \mathbf{p}_d)$ , the singularity appears when  $\det(J(\mathbf{e}, \mathbf{p}_d)) = -|\cos(\psi_e)|^2 = 0 \implies |\psi_e| = (\pi/2)$ . On the other hand, we have that the angle  $\psi_e$  is the pointing angle of the vehicle to the target trajectory. Therefore, a configuration where  $|\psi_e| > \pi/2$  will not be singular, but the vehicle, in this case, will face the desired trajectory from the opposite side. In this respect, we select and impose the feasible error configuration set in (19), in order to guarantee that: 1) the system is in a nonsingular configuration and 2) the vehicle is facing directly the target trajectory.

*Remark 4:* It should be noted that the constraint set  $\mathcal{E}$  in (19) guarantees that  $J(\mathbf{e}, \mathbf{p}_d)$  is nonsingular. Thus, there exists strictly positive constants  $\underline{J}$  and  $\bar{J}$  such that, respectively

$$\lambda_{\min}\left(\frac{J(\cdot) + J^\top(\cdot)}{2}\right) \geq \underline{J} > 0 \text{ and } \|J(\cdot)\| \leq \bar{J}.$$

Now, in view of (17) and considering the perturbed dynamic equations of (3a)–(3c), the uncertain transformed kinematics/dynamics of the systems can be given as follows:

$$\dot{\mathbf{e}} = J(\mathbf{e}, \mathbf{p}_d) \mathbf{v} + \zeta(\mathbf{e}, \dot{\mathbf{p}}_d) + \xi(\mathbf{e}, v) \quad (20a)$$

$$\dot{\mathbf{v}} = \mathbf{M}^{-1} [\tau + \mathbf{C}(\mathbf{v}, v) \mathbf{v} + \mathbf{D}(\mathbf{v}) \mathbf{v} + \mathbf{g}] + \xi \quad (20b)$$

$$\dot{v} = \frac{1}{m_{22}} [-m_{11} u r + Y_v v + Y_{v|v}|v|v] + \delta_Y. \quad (20c)$$

The corresponding nominal dynamics (i.e.,  $\xi = \mathbf{0}$ ) are now given by

$$\dot{\hat{\mathbf{e}}} = J(\hat{\mathbf{e}}, \mathbf{p}_d) \hat{\mathbf{v}} + \zeta(\hat{\mathbf{e}}, \dot{\hat{\mathbf{p}}}_d) + \xi(\hat{\mathbf{e}}, \hat{v}) \quad (21a)$$

$$\dot{\hat{\mathbf{v}}} = \mathbf{M}^{-1} [\hat{\tau} + \mathbf{C}(\hat{\mathbf{v}}, \hat{v}) \hat{\mathbf{v}} + \mathbf{D}(\hat{\mathbf{v}}) \hat{\mathbf{v}} + \mathbf{g}] \quad (21b)$$

$$\dot{\hat{v}} = \frac{1}{m_{22}} [-m_{11} \hat{u} \hat{r} + Y_{\hat{v}} \hat{v} + Y_{v|\hat{v}} |\hat{v}| \hat{v}]. \quad (21c)$$

It should be noticed that we use the  $(\hat{\cdot})$  notation for the nominal state in order to account for the mismatch between the real state and the nominal one that will be used in the following analysis.

### B. State Feedback Design

Consider the feedback law

$$\boldsymbol{\tau} = \hat{\tau}(\hat{\mathbf{e}}, \hat{v}) + \kappa(\mathbf{e}, \hat{\mathbf{e}}, \mathbf{v}, \hat{v}) \quad (22)$$

which consists of a nominal control action  $\hat{\tau}(\hat{\mathbf{e}}, \hat{v}) \in T$  and a state feedback law  $\kappa : \mathbb{R}^3 \times \mathbb{R}^3 \rightarrow T$ . The control action  $\hat{\tau}(\hat{\mathbf{e}}, \hat{v})$  will be the outcome of an FHOCP solved for the nominal dynamics (21), while the state feedback law  $\kappa(\cdot)$  is designed in order to guarantee that the real trajectories  $\mathbf{e}(t)$  and  $\mathbf{v}(t)$  [i.e., the solution of (20)] always remain inside a

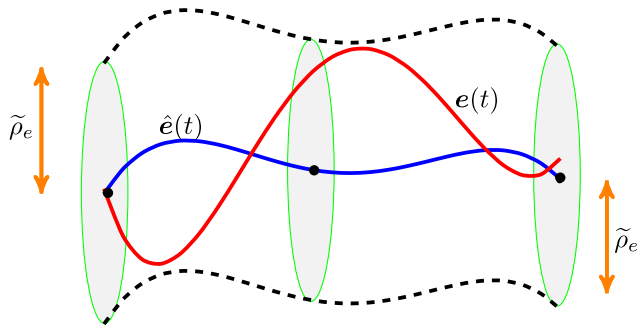


Fig. 5. Tube centered along the trajectory  $\hat{e}(t)$  (depicted by the blue line) with radius  $\tilde{\rho}_e$ . Under the proposed control law, the real trajectory  $e(t)$  (depicted with red line) lies inside the tube for all times, i.e.,  $\|\rho_e(t)\| \leq \tilde{\rho}_e \forall t \in \mathbb{R}_{\geq 0}$ .

bounded tube centered along the nominal trajectories  $\hat{e}(t)$  and  $\hat{v}(t)$  i.e., the solution of (21). Now, let us define by  $\rho_e(t)$  and  $\rho_v(t)$  the discrepancy between the real errors and the nominal ones, given as

$$\rho_e(t) := e(t) - \hat{e}(t) \quad (23a)$$

$$\rho_v(t) := v(t) - \hat{v}(t) \quad (23b)$$

with  $\rho_e(0) = e(0) - \hat{e}(0) = \mathbf{0}$  and  $\rho_v(0) = v(0) - \hat{v}(0) = \mathbf{0}$ , respectively. In view of (23a), the dynamics of  $\rho_e(t)$  are given as

$$\begin{aligned} \dot{\rho}_e &= \dot{e} - \dot{\hat{e}} \\ &= J(\mathbf{e}, \mathbf{p}_d)v - J(\hat{e}, \mathbf{p}_d)\hat{v} + \zeta(\mathbf{e}, \dot{\mathbf{p}}_d) - \zeta(\hat{e}, \dot{\mathbf{p}}_d) \\ &\quad + \zeta(\mathbf{e}, v) - \zeta(\hat{e}, \hat{v}). \end{aligned} \quad (24)$$

By adding and subtracting the term  $J(\mathbf{e}, \mathbf{p}_d)\hat{v}$  and by defining the function

$$h_e(\mathbf{e}, \hat{v}) := J(\mathbf{e}, \mathbf{p}_d)\hat{v}$$

for which it also holds that:

$$h_e(\hat{e}, \hat{v}) := J(\hat{e}, \mathbf{p}_d)\hat{v}$$

(24) becomes

$$\begin{aligned} \dot{\rho}_e &= h_e(\mathbf{e}, \hat{v}) - h_e(\hat{e}, \hat{v}) + J(\mathbf{e}, \mathbf{p}_d)\rho_v + \zeta(\mathbf{e}, \dot{\mathbf{p}}_d) - \zeta(\hat{e}, \dot{\mathbf{p}}_d) \\ &\quad + \zeta(\mathbf{e}, v) - \zeta(\hat{e}, \hat{v}). \end{aligned} \quad (25)$$

Note that for the continuously differentiable functions  $h_e(\cdot)$ ,  $\zeta(\cdot)$  and  $\xi(\cdot)$ , the following holds:

$$\|h_e(\mathbf{e}, \hat{v}) - h_e(\hat{e}, \hat{v})\| \leq \mathcal{L}_1 \|\mathbf{e} - \hat{e}\| = \mathcal{L}_1 \|\rho_e\| \quad (26a)$$

$$\|\zeta(\mathbf{e}, \dot{\mathbf{p}}_d) - \zeta(\hat{e}, \dot{\mathbf{p}}_d)\| \leq \mathcal{L}_2 \|\mathbf{e} - \hat{e}\| = \mathcal{L}_2 \|\rho_e\| \quad (26b)$$

$$\begin{aligned} \|\zeta(\mathbf{e}, v) - \zeta(\hat{e}, \hat{v})\| &\leq \mathcal{L}_3 \|\mathbf{e} - \hat{e}\| + \mathcal{L}_4 \|v - \hat{v}\| \\ &= \mathcal{L}_3 \|\rho_e\| + \mathcal{L}_4 \|\rho_v\| \end{aligned} \quad (26c)$$

where  $\mathcal{L}_1, \mathcal{L}_2, \mathcal{L}_3, \mathcal{L}_4 > 0$  stand for their Lipschitz constants.

The time derivative of the signal  $\rho_v$  in view of (23b) is given as

$$\dot{\rho}_v = \dot{v} - \dot{\hat{v}} = \mathbf{M}^{-1}(\boldsymbol{\tau} - \hat{\boldsymbol{\tau}}) + \varphi(\mathbf{v}, v) - \varphi(\hat{\mathbf{v}}, \hat{v}) + \boldsymbol{\xi} \quad (27)$$

where for the continuously differentiable function

$$\varphi(\mathbf{v}, v) := \mathbf{M}^{-1}[\mathbf{C}(\mathbf{v}, v)\mathbf{v} + \mathbf{D}(\mathbf{v})\mathbf{v} + \mathbf{g}]$$

$$\varphi(\hat{\mathbf{v}}, \hat{v}) := \mathbf{M}^{-1}[\mathbf{C}(\hat{\mathbf{v}}, \hat{v})\hat{\mathbf{v}} + \mathbf{D}(\hat{\mathbf{v}}, \hat{v})\hat{\mathbf{v}} + \mathbf{g}]$$

it holds that

$$\begin{aligned} \|\varphi(\mathbf{v}, v) - \varphi(\hat{\mathbf{v}}, \hat{v})\| &\leq \mathcal{L}_5 \|\mathbf{v} - \hat{\mathbf{v}}\| + \mathcal{L}_6 \|\mathbf{v} - \hat{\mathbf{v}}\| \\ &= \mathcal{L}_5 \|\rho_v\| + \mathcal{L}_6 \|\mathbf{v} - \hat{\mathbf{v}}\|. \end{aligned} \quad (28)$$

It will be proven, thereafter, that for the unactuated velocities  $v$  and  $\hat{v}$ , it holds that

$$\|\mathbf{v} - \hat{\mathbf{v}}\| \leq \bar{v} + \hat{v} \quad (29)$$

where  $\bar{v}$  and  $\hat{v}$  to be defined in Section IV-C. Now, based on the aforementioned analysis, the following Lemma can be stated.

**Lemma 1:** The state feedback law

$$\kappa(\mathbf{e}, \hat{\mathbf{e}}, \mathbf{v}, \hat{\mathbf{v}}) := -k\sigma(\mathbf{e} - \hat{\mathbf{e}}) - \sigma(\mathbf{v} - \hat{\mathbf{v}}) \quad (30)$$

where the gains are chosen such that

$$k := \frac{\underline{k} + \mathcal{L}_4(\bar{v} + \hat{v})}{\lambda_{\min}(J)}, \quad \underline{k} > 0, \quad \varpi > \frac{\alpha_1}{4\underline{k}}, \quad \sigma > \frac{\alpha_1 \varpi + \alpha_2}{\lambda_{\min}(\mathbf{M}^{-1})} \quad (31a)$$

$$\alpha_1 := \mathcal{L} + k\mathcal{L}_5 + k\mathcal{L}_6(\bar{v} + \hat{v}), \quad \alpha_2 := \mathcal{L}_5 + \mathcal{L}_6(\bar{v} + \hat{v}) + \bar{J} \quad (31b)$$

renders the sets

$$\mathcal{Z}_1 = \left\{ \rho_e : \|\rho_e\| \leq \tilde{\rho}_e := \frac{\xi}{\min\{\varsigma_1, \varsigma_2\}} \right\} \quad (32a)$$

$$\mathcal{Z}_2 = \left\{ \rho_v : \|\rho_v\| \leq \tilde{\rho}_v := \frac{(1+k)\xi}{\min\{\varsigma_1, \varsigma_2\}} \right\}. \quad (32b)$$

RCI sets for the error dynamics (25) and (27), where the constants  $\varsigma_1$  and  $\varsigma_2$  are given by

$$\varsigma_1 := \underline{k} - \frac{\alpha_1}{4\varpi} > 0, \quad \varsigma_2 := \sigma \lambda_{\min}(\mathbf{M}^{-1}) - \alpha_1 \varpi - \alpha_2 > 0. \quad (33)$$

**Proof:** A baskstepping control design technique will be adopted. The signal  $\rho_e$  in (25) can be seen as the virtual control input to be designed in ordered to stabilize the system (25). Consider the positive definite function  $\Lambda_1(\rho_e) = (1/2)\|\rho_e\|^2$ . The time derivative of  $\Lambda_1$  along the solutions of system (25) is given by

$$\begin{aligned} \dot{\Lambda}_1(\rho_e) &= \rho_e^\top [h(\mathbf{e}, \mathbf{v}) - h(\hat{\mathbf{e}}, \hat{\mathbf{v}})] + \rho_e^\top [\zeta(\mathbf{e}, \dot{\mathbf{p}}_d) - \zeta(\hat{\mathbf{e}}, \dot{\mathbf{p}}_d)] \\ &\quad + \rho_e^\top J(\mathbf{e}, \mathbf{p}_d)\rho_v + \rho_e^\top [\zeta(\mathbf{e}, v) - \zeta(\hat{\mathbf{e}}, \hat{v})] \\ &\leq \mathcal{L}_1 \|\rho_e\|^2 + \mathcal{L}_2 \|\rho_e\|^2 + \rho_e^\top J(\mathbf{e}, \mathbf{p}_d)\rho_v \\ &\quad + \mathcal{L}_3 \|\rho_e\|^2 + \mathcal{L}_4(\bar{v} + \hat{v}) \\ &= \mathcal{L} \|\rho_e\|^2 + \rho_e^\top J(\mathbf{e}, \mathbf{p}_d)\rho_v + \mathcal{L}_4(\bar{v} + \hat{v}) \end{aligned}$$

where  $\mathcal{L} := \mathcal{L}_1 + \mathcal{L}_2 + \mathcal{L}_3$ . By designing the virtual control input as  $\rho_v = -k\rho_e$ , where  $k := (\underline{k} + \underline{k} + \mathcal{L}_4(\bar{v} + \hat{v})) / (\lambda_{\min}(J))$ ,  $\underline{k} > 0$ , it holds that

$$\begin{aligned} \dot{\Lambda}_1(\rho_e) &\leq \mathcal{L} \|\rho_e\|^2 - k \rho_e^\top J(\mathbf{e}, \mathbf{p}_d)\rho_e + \mathcal{L}_4(\bar{v} + \hat{v}) \\ &\leq \mathcal{L} \|\rho_e\|^2 - k \lambda_{\min}(J) \|\rho_e\|^2 + \mathcal{L}_4(\bar{v} + \hat{v}) \\ &= -[k \lambda_{\min}(J) - \mathcal{L}] \|\rho_e\|^2 + \mathcal{L}_4(\bar{v} + \hat{v}) \\ &= -\underline{k} \|\rho_e\|^2 + \mathcal{L}_4(\bar{v} + \hat{v}). \end{aligned}$$

By taking the aforementioned virtual control design into consideration, define the backstepping auxiliary vector by

$$\boldsymbol{\varrho} := \rho_v + k\rho_e, \quad \mathbf{n} := [\rho_e^\top, \boldsymbol{\varrho}^\top]^\top$$

and consider the function  $\Lambda(\mathbf{n}) := (1/2)\|\mathbf{n}\|^2$ . Then, the time derivative of  $\Lambda(\mathbf{n})$  is given by

$$\begin{aligned}\dot{\Lambda}(\mathbf{n}) &= \rho_e^\top \dot{\rho}_e + \boldsymbol{\varrho}^\top \dot{\boldsymbol{\varrho}} \\ &= \rho_e^\top \dot{\rho}_e + \boldsymbol{\varrho}^\top [\dot{\rho}_v + k\dot{\boldsymbol{\varrho}}_e] \\ &= [\rho_e + k\boldsymbol{\varrho}]^\top \dot{\rho}_e + \boldsymbol{\varrho}^\top [\varphi(\mathbf{v}, \mathbf{v}) - \varphi(\hat{\mathbf{v}}, \hat{\mathbf{v}})] \\ &\quad + \boldsymbol{\varrho}^\top \mathbf{M}^{-1}(\boldsymbol{\tau} - \hat{\boldsymbol{\tau}}) + \boldsymbol{\varrho}^\top \tilde{\boldsymbol{\xi}}.\end{aligned}\quad (34)$$

By using the fact that

$$xy \leq \frac{1}{\varpi}x^2 + \varpi y^2$$

for every  $x, y \in \mathbb{R}$ ,  $\varpi > 0$ , we get

$$\|\rho_e\| \|\boldsymbol{\varrho}\| \leq \frac{1}{4\varpi} \|\rho_e\|^2 + \varpi \|\boldsymbol{\varrho}\|^2.$$

By using the latter, (34) becomes

$$\begin{aligned}\dot{\Lambda}(\mathbf{n}) &\leq -\left(\underline{k} - \frac{\alpha_1}{4\varpi}\right) \|\rho_e\|^2 + (\alpha_1 \varpi + \alpha_2) \|\boldsymbol{\varrho}\|^2 \\ &\quad + \boldsymbol{\varrho}^\top \mathbf{M}^{-1}(\boldsymbol{\tau} - \hat{\boldsymbol{\tau}}) + \|\mathbf{n}\| \tilde{\boldsymbol{\xi}}\end{aligned}\quad (35)$$

with  $\alpha_1$  and  $\alpha_2$  given in (31a). By designing

$$\boldsymbol{\tau} - \hat{\boldsymbol{\tau}} = -\sigma \boldsymbol{\varrho} = -k\sigma(\mathbf{e} - \hat{\mathbf{e}}) - \sigma(\mathbf{v} - \hat{\mathbf{v}})$$

which is compatible with (30), we get

$$\begin{aligned}\dot{\Lambda}(\mathbf{n}) &\leq -\left(\underline{k} - \frac{\alpha_1}{4\varpi}\right) \|\rho_e\|^2 + (\alpha_1 \varpi + \alpha_2) \|\boldsymbol{\varrho}\|^2 \\ &\quad - \sigma \boldsymbol{\varrho}^\top \mathbf{M}^{-1} \boldsymbol{\varrho} + \|\mathbf{n}\| \tilde{\boldsymbol{\xi}} \\ &\leq -\left(\underline{k} - \frac{\alpha_1}{4\varpi}\right) \|\rho_e\|^2 + (\alpha_1 \varpi + \alpha_2) \|\boldsymbol{\varrho}\|^2 \\ &\quad - \sigma \lambda_{\min}(\mathbf{M}^{-1}) \|\boldsymbol{\varrho}\|^2 + \|\mathbf{n}\| \tilde{\boldsymbol{\xi}} \\ &= -\left(\underline{k} - \frac{\alpha_1}{4\varpi}\right) \|\rho_e\|^2 - [\sigma \lambda_{\min}(\mathbf{M}^{-1}) - \alpha_1 \varpi - \alpha_2] \|\boldsymbol{\varrho}\|^2 \\ &\quad + \|\mathbf{n}\| \tilde{\boldsymbol{\xi}} \\ &= -\varsigma_1 \|\rho_e\|^2 - \varsigma_2 \|\boldsymbol{\varrho}\|^2 + \|\mathbf{n}\| \tilde{\boldsymbol{\xi}} \\ &\leq -\min\{\varsigma_1, \varsigma_2\} \|\mathbf{n}\|^2 + \|\mathbf{n}\| \tilde{\boldsymbol{\xi}} \\ &\leq -\|\mathbf{n}\| [\min\{\varsigma_1, \varsigma_2\} \|\mathbf{n}\| - \tilde{\boldsymbol{\xi}}]\end{aligned}\quad (36)$$

with  $\varsigma_1, \varsigma_2$  as given in (33). Thus,  $\Lambda(\mathbf{n}) < 0$ , when

$$\|\mathbf{n}\| > \frac{\tilde{\boldsymbol{\xi}}}{\min\{\varsigma_1, \varsigma_2\}}.$$

Taking the latter into consideration and the fact that  $\mathbf{n}(0) = 0$ , it holds that

$$\|\mathbf{n}(t)\| \leq \frac{\tilde{\boldsymbol{\xi}}}{\min\{\varsigma_1, \varsigma_2\}} \quad \forall t \geq 0.$$

Moreover, the following inequalities hold:

$$\begin{aligned}\|\rho_e\| &\leq \|\mathbf{n}\| \Rightarrow \|\rho_e(t)\| \leq \frac{\tilde{\boldsymbol{\xi}}}{\min\{\varsigma_1, \varsigma_2\}} \quad \forall t \geq 0 \\ \|\rho_v\| - k\|\rho_e\| &\leq \|\rho_v + k\rho_e\| = \|\boldsymbol{\varrho}\| \leq \|\mathbf{n}\| \\ &\Rightarrow \|\rho_v(t)\| \leq \frac{(1+k)\tilde{\boldsymbol{\xi}}}{\min\{\varsigma_1, \varsigma_2\}} \quad \forall t \geq 0\end{aligned}$$

which concludes the proof. ■

A graphical illustration of the proposed tube-based control strategy is given in Fig. 5. Under the proposed control scheme (22), the real trajectory  $\mathbf{e}(t)$  lies inside the tube, which is centered along the nominal trajectory  $\hat{\mathbf{e}}$  with radius  $\tilde{\rho}_e$  for all times, i.e.,  $\|\rho_e(t)\| \leq \tilde{\rho}_e \quad \forall t \in \mathbb{R}_{\geq 0}$ .

### C. Bounds on the Unactuated Velocity $v$

In the sequel, we will prove the boundedness of the unactuated velocity  $v$  along the sway direction. Let us define the positive definite and radially unbounded function  $V_v = (1/2)m_{22}v^2$ , where  $m_{22}$  denotes the vehicle's mass/added mass of inertia of the sway degree of freedom [see (1f)]. Differentiating  $V_v$  with respect to time and substituting (1f), we obtain

$$\begin{aligned}\dot{V}_v &= m_{22}v\dot{v} \\ &= -m_{11}uvr + Y_v v^2 + Y_{v|v|} v^2 |v| + vm_{22}\delta_Y\end{aligned}$$

which after algebraic manipulations, and using the facts  $Y_v, Y_{v|v|} < 0$  and  $|\delta_Y| \leq \bar{\delta}_Y$ , leads to

$$\dot{V}_v \leq Y_{v|v|} |v|^3 + Y_v |v|^2 + m_{11}\bar{u}\bar{r}|v| + m_{22}\bar{\delta}_Y|v|.$$

Therefore, we conclude that  $\dot{V}_v$  is negative when

$$|v| > \sqrt{\mathfrak{a} + \mathfrak{b} + \mathfrak{c}}$$

where  $\mathfrak{a} \triangleq ((Y_v)/(2Y_{v|v|}))^2$ ,  $\mathfrak{b} \triangleq (m_{11}\bar{u}\bar{r} + m_{22}\bar{\delta}_Y)/(-Y_{v|v|})$ , and  $\mathfrak{c} \triangleq -(Y_v)/(2Y_{v|v|})$ . Consequently, we have

$$|v(t)| \leq \bar{v} := \max\left\{|v(0)|, \frac{\sqrt{\mathfrak{a} + \mathfrak{b}} - \mathfrak{c}}{m_{22}}\right\} \quad \forall t \geq 0 \quad (37)$$

which intuitively means that for any underactuated underwater vehicle and for any bounded velocities  $|u| \leq \bar{u}$ ,  $|w| \leq \bar{w}$  and  $|r| \leq \bar{r}$ , the velocity  $v$  in the unactuated sway direction remains bounded by an upper bound that depends on: 1) the upper bounds  $\bar{u}$ ,  $\bar{w}$ , and  $\bar{r}$ ; 2) the parameters of the dynamic model (1); and 3) the magnitude of the external disturbances. In a similar way, by defining a positive definite and radially unbounded function  $V_{\hat{v}} = (1/2)m_{22}\hat{v}^2$ , we can calculate an upper bound for the nominal velocity  $\hat{v}$  given as

$$|\hat{v}(t)| \leq \hat{v} := \max\left\{|\hat{v}(0)|, \frac{\sqrt{\mathfrak{a} + \hat{\mathfrak{b}}} - \mathfrak{c}}{m_{22}}\right\} \quad \forall t \quad (38)$$

where  $\hat{\mathfrak{b}} \triangleq (m_{11}\bar{u}\bar{r}/ - Y_{v|v|})$ .

### D. Online Optimal Control

As mentioned earlier, the control action  $\hat{\boldsymbol{\tau}}(\hat{\mathbf{e}}, \hat{\mathbf{v}})$  in (22) will be the outcome of an FHOCP solved for the nominal dynamics (21). In this respect, consider a sequence of sampling times  $\{t_k\}$ ,  $k \in \mathbb{N}$ , with a constant sampling period  $0 < \mathfrak{t} < N$ , where  $N$  is a prediction horizon such that  $t_{k+1} := t_k + \mathfrak{t} \quad \forall k \in \mathbb{N}$ . At each sampling time  $t_k$ , an FHOCP is solved as follows:

$$\min_{\hat{\boldsymbol{\tau}}(\cdot)} \left\{ \|\hat{\mathbf{e}}(t_k + N)\|_P^2 + \int_{t_k}^{t_k+N} [\|\hat{\mathbf{e}}(\mathfrak{s})\|_Q^2 + \|\hat{\boldsymbol{\tau}}(\mathfrak{s})\|_R^2] d\mathfrak{s} \right\} \quad (39a)$$

$$\text{subject to: } \dot{\hat{\mathbf{x}}}(\mathfrak{s}) = g(\mathbf{x}(\mathfrak{s}), \hat{\boldsymbol{\tau}}(\mathfrak{s})), \quad \hat{\mathbf{x}}(t_k) = \mathbf{x}(t_k) \quad (39b)$$

$$\hat{\mathbf{x}}(\mathfrak{s}) \in \widetilde{\mathcal{E}} \times \widetilde{\mathcal{V}}, \quad \hat{\boldsymbol{\tau}}(\mathfrak{s}) \in \widetilde{\mathcal{T}} \quad \forall \mathfrak{s} \in [t_k, t_k + N] \quad (39c)$$

$$\hat{\mathbf{x}}(t_k + N) \in \mathcal{F} \quad (39d)$$

where

$$\boldsymbol{\chi} := [\mathbf{e}^\top, \mathbf{v}^\top, v]^\top \in \mathbb{R}^6$$

$$g(\boldsymbol{\chi}, \boldsymbol{\tau}) := \begin{bmatrix} J(\hat{\mathbf{e}}, \mathbf{p}_d) \hat{\mathbf{v}} + \zeta(\hat{\mathbf{e}}, \dot{\mathbf{p}}_d) + \xi(\hat{\mathbf{e}}, \hat{\mathbf{v}}) \\ \mathbf{M}^{-1}(\hat{\boldsymbol{\tau}} + \mathbf{C}(\hat{\mathbf{v}}, \hat{\mathbf{v}}) \hat{\mathbf{v}} - \mathbf{D}(\hat{\mathbf{v}}) \hat{\mathbf{v}} - \mathbf{g}) \\ \frac{1}{m_{22}} [-m_{11}\hat{u}\hat{r} + Y_v \hat{v} + Y_{v|v|} |\hat{v}| \hat{v}] \end{bmatrix}$$

TABLE I  
VEHICLE DYNAMIC PARAMETER SET

$m_{11}$	$m_{22}$	$m_{33}$	$m_{44}$
21.5	26.5	26.5	8.0
$X_u$	$Y_v$	$Z_w$	$N_r$
-70.0	-100.0	-100.0	-50.0
$X_{ u u}$	$Y_{ v v}$	$Z_{ w w}$	$N_{ r r}$
-100.0	-200.0	-200.0	-100.0
$W$	$B$		
176.6N	181.2N		

and  $Q$ ,  $P \in \mathbb{R}^{6 \times 6}$  and  $R \in \mathbb{R}^{3 \times 3}$  are positive definite gain matrices. Moreover,  $\tilde{\mathcal{E}}$ ,  $\tilde{\mathcal{V}}$ , and  $\mathcal{F}$  are designing sets that are defined in order to guarantee that while the solution of the FHOCP (39a)–(39d) is derived for the nominal dynamics (21), the real trajectory  $\chi(t)$  and control inputs  $\tau(t)$  satisfy the corresponding state and input constraints. More specifically, the following modifications are performed:

$$\tilde{\mathcal{E}} := \mathcal{E} \ominus \mathcal{Z}_1, \quad \tilde{\mathcal{V}} := V \ominus \mathcal{Z}_2, \quad \tilde{T} := T \ominus [\mathfrak{K} \circ \tilde{\mathcal{Z}}]$$

where

$$\mathfrak{K} := \text{diag}\{-k\sigma I_3, -\sigma I_3\}, \quad \tilde{\mathcal{Z}} := \mathcal{Z}_1 \times \mathcal{Z}_2.$$

This intuitively means that the sets  $\mathcal{E}$  and  $V$  are tightened accordingly in order to guarantee that while the nominal states  $\hat{e}$  and  $\hat{v}$  and the nominal control input  $\hat{\tau}$  are calculated, the corresponding real states  $e$  and  $v$  and real control input  $\tau$  satisfy the state and input constraints  $\mathcal{E}$ ,  $V$ , and  $T$ , respectively.<sup>2</sup> Define the terminal set by

$$\mathcal{F} := \{\hat{\chi} \in \tilde{\mathcal{E}} : \|\hat{\chi}\|_P \leq \bar{\epsilon}\}, \quad \bar{\epsilon} > 0 \quad (40)$$

which is employed here in order to enforce the stability of the system [33].

*Newly Detected Obstacles:* As mentioned earlier, the obstacles within the workspace may be detected online by the vehicle's onboard sensors (e.g., multibeam imaging or side scan sonar). In such a case, it should be assured that the solution of the FHOCP corresponds to the region that is accessible by the sensing capabilities of the vehicle. This intuitively means that at the time of sampling  $t_k$  when solving the FHOCP, any new obstacles have been taken into account by the controller even for the scenario with maximum running speed (i.e., a case when vehicle moves with its maximum speed under maximum disturbances, which is tangent to robot's moving direction.). Thus, recalling that  $\bar{R}$  denotes the sensing range of the system, as already stated in Section III-B, the prediction horizon is set as follows:

$$N \leq \frac{\bar{R}}{\max\{\bar{u}, \bar{w}, \bar{r}\} + \tilde{\mathcal{Z}}} \quad (41)$$

where  $\bar{u}$ ,  $\bar{w}$ , and  $\bar{r}$  are defined in (7).

<sup>2</sup>This constitutes a standard constraints set modification technique adopted in tube-based NMPC frameworks. For more details, see [36].

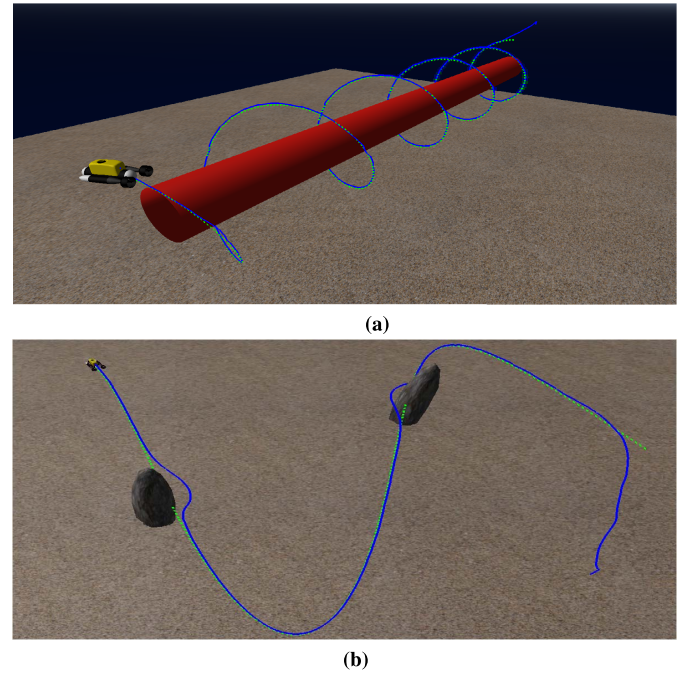


Fig. 6. Evolution of the proposed methodology in two separate scenarios. (a) Obstacle-free scenario and (b) constrained workspace scenario, including obstacles. In obstacle-free scenario, an inspection task along a pipeline structure was considered, while, in the constrained scenario, the tracking control problem was considered in a workspace, including two obstacles. The trace of the vehicle and the desired trajectory are depicted by blue and green lines, respectively. The desired trajectory coincides with obstacles positions. The obstacles are detected and considered to the controller when they are within the sensing range  $\bar{R}$ . The robot has been left the desired trajectory when it is needed in order to avoid the obstacles.

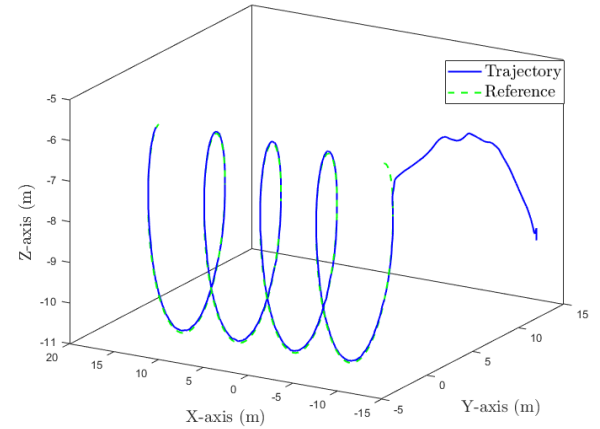


Fig. 7. Obstacle-free scenario: the 3-D evolution of the vehicle and desired trajectory.

*Remark 5:* It should be noticed that in a real scenario, AUVs use sonar sensors to obtain knowledge about the environment. The detection range of these sonar sensors (i.e.,  $\bar{R}$ ) depends on many factors, including the frequency. Low-frequency sonars can detect objects at very long distance, depending on the sound propagation environment. Medium frequency sonars (typically operating between 7.5 and up to 30 kHz) can detect an object at a multiple nautical miles. On the other hand, high-frequency sonars (>100 kHz)

**Algorithm 1** Implementation of Feedback Control Laws  $\tau(t)$ 

**Step 1:** At time  $t_k$ , the current state of the robot (i.e.,  $\eta(t_k)$ ,  $v(t_k)$ ) is measured, the errors  $e_d(t_k)$ ,  $e_z(t_k)$  and  $e_o(t_k)$  of (11)–(13) are designed, and  $e(t_k) = \hat{e}(t_k)$  and  $v(t_k) = \hat{v}(t_k)$  are set.

**Step 2:** Based on  $(e(t_k), \hat{e}(t_k))$  and  $(v(t_k), \hat{v}(t_k))$  solve FHOCP (39a)–(39d) to obtain the nominal control action  $\hat{\tau}(t_k)$  and the actual control action  $\tau(t_k) = \hat{\tau}(t_k) + \kappa_i(e(t_k), \hat{e}(t_k), v(t_k), \hat{v}(t_k))$ .

**Step 3:** Apply the control  $\tau(t_k)$  to the system, during sampling interval  $[t_k, t_{k+1})$ , where  $t_{k+1} = t_k + t$ .

**Step 4:** Measure the state of the system at the next time instant  $t_{k+1}$ , and set  $t_k \leftarrow t_{k+1}$ ; **Go to Step 1.**

typically used for underwater inspection can detect smaller objects at a few hundreds of meters (i.e.,  $>100$  m). Thus, in view of (7), in a real scenario, the predefined upper bound of the vehicle velocity can be tuned accordingly to the capability sensing range  $\tilde{R}$  of the available sonar system (i.e., by selecting lower values for the velocity constraints in (7), with respect to the original given upper bounds) in order to get a valuable prediction horizon enough for solving the FHOCP (39a)–(39d).

The pseudocode description of the proposed real-time control scheme is given in Algorithm 1. Now, we are ready to state the main result of this work.

**Theorem 1:** Suppose that, at time  $t = 0$ , the FHOCP [see (39a)–(39d)] is feasible. Then, the proposed feedback control law [see (22) and (30)] renders the closed-loop system ISS with respect to the disturbances, for every initial condition  $\hat{x}(0) \in \mathcal{E}$ .

*Proof:* The proof of the theorem follows similar arguments presented in our previous work [37]. Due to the fact that only the state of the nominal system is used, while the FHOCP (39a)–(39d) is solved, the online optimization does not depend on the disturbances. The proof of feasibility, follows same arguments as in [33] and [37],<sup>3</sup> which leads to

$$x(t_{k+1} + s; \hat{\tau}(\cdot), x(t_{k+1})) \in \mathcal{E} \times \mathcal{V} \quad \forall s \in [0, N].$$

By taking the aforementioned into consideration, the feasibility of a solution to the optimization problem at time  $t_k$  implies feasibility at all times  $t_{n+1}$  with  $n > k$ . Thus, since, at time  $t = 0$ , a solution is assumed to be feasible, a solution to the optimal control problem is feasible for all  $t \in \mathbb{R}_{\geq 0}$ . Regarding the convergence analysis, due to the fact that the sets  $\mathcal{Z}_1$  and  $\mathcal{Z}_2$  are RPI sets, it holds that

$$\|\rho_e(t)\| \leq \tilde{\rho}_e \quad \forall t \geq 0 \quad (42)$$

$$\|\rho_v(t)\| \leq \tilde{\rho}_v \quad \forall t \geq 0 \quad (43)$$

where

$$\tilde{\rho}_e := \frac{\bar{\xi}}{\min\{\zeta_1, \zeta_2\}}, \quad \tilde{\rho}_v := \frac{(1+k)\bar{\xi}}{\min\{\zeta_1, \zeta_2\}}.$$

<sup>3</sup>The analytical proof of feasibility is outside the scope of this work and has been omitted.

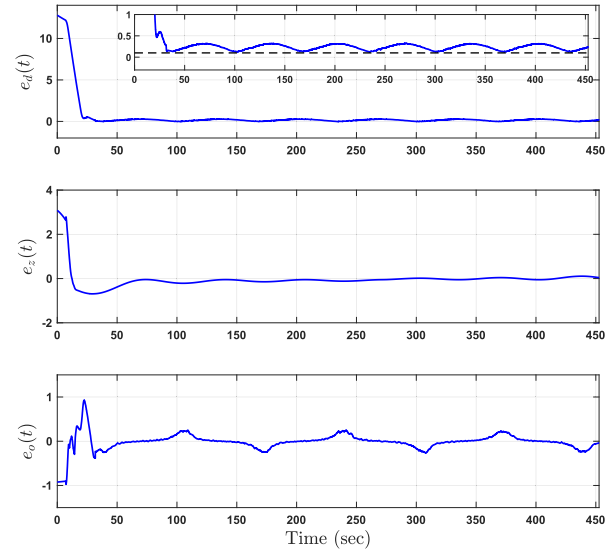


Fig. 8. Obstacle-free scenario: the evolution of the transformed errors.

Since only the nominal system dynamics (21) are used for the online computation of the control actions  $\hat{\tau}(s) \in \tilde{\mathcal{T}}$  and  $s \in [t_k, t_k + N]$  through the FHOCP (39a)–(39d), by invoking nominal NMPC stability results found on [33], it can be proven that the NMPC control law  $\hat{\tau}$  renders the closed-loop trajectories of the nominal system (21) asymptotically ultimated bounded in the sets  $\mathcal{F}$  [38]. Then, from [28, Lemma 4.5, p. 150], there exist class  $\mathcal{KL}$  functions  $\beta_e$  and  $\beta_v$  such that

$$\|\hat{e}(t)\| \leq \beta_e(\|\hat{e}(0)\|, t) \quad \forall t \in \mathbb{R}_{\geq 0} \quad (44)$$

$$\|\hat{v}(t)\| \leq \beta_v(\|\hat{v}(0)\|, t) \quad \forall t \in \mathbb{R}_{\geq 0}. \quad (45)$$

By combining (23) and (42)–(45), we get

$$\|e(t)\| \leq \beta_e(\|e(0)\|, t) + \tilde{\rho}_e \quad \forall t \in \mathbb{R}_{\geq 0}$$

$$\|v(t)\| \leq \beta_v(\|\hat{v}(0)\|, t) + \tilde{\rho}_v \quad \forall t \in \mathbb{R}_{\geq 0}.$$

Thus, we have shown that the proposed control law [see (22) and (30)] renders the closed-loop system ISS with reference to the disturbances  $\xi(t) \in \Xi$ , for every initial condition  $x(0) \in X$  and  $v(0) \in V$ , which leads to the conclusion of the proof. ■

**Remark 6:** Regarding the tube's design parameters, by observing (31)–(33), the parameters  $\bar{J}$ ,  $\lambda_{\min}(M^{-1})$ , and  $\lambda_{\min}(J)$  are initially given. Then, according to the given dynamics and state constraints, the Lipschitz constants  $\mathcal{L}_1, \dots, \mathcal{L}_6$  are computed. Then, we tune the parameter gain  $k > 0$ , and subsequently, we tune the remaining three control gains  $k$ ,  $\varpi$ , and  $\sigma$  such that the inequalities in (31a) are satisfied.

In Fig. 10, the vehicle velocities are presented, and respective constraints are satisfied. Finally, in Fig. 11, the vehicle's thruster inputs are shown. As it can be seen, the input constraints are also satisfied.

## V. SIMULATION RESULTS

Real-time simulations have been performed to demonstrate the efficiency of the proposed approach. The simulation environment was designed based on UwSim dynamic simulator

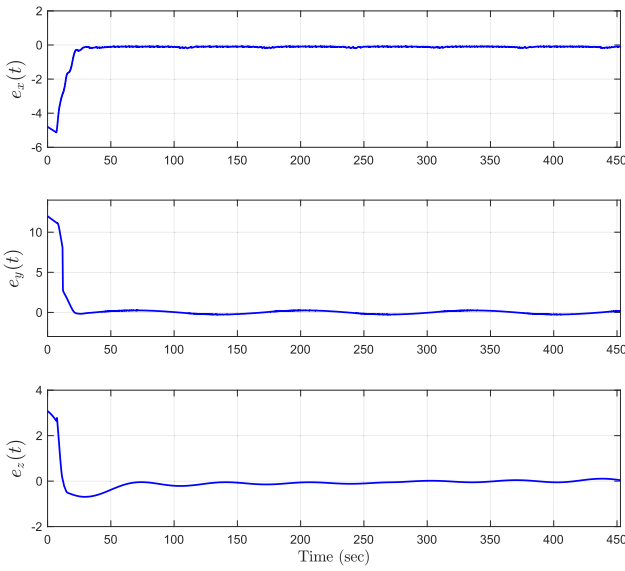


Fig. 9. Obstacle-free scenario: the evolution of the real errors.

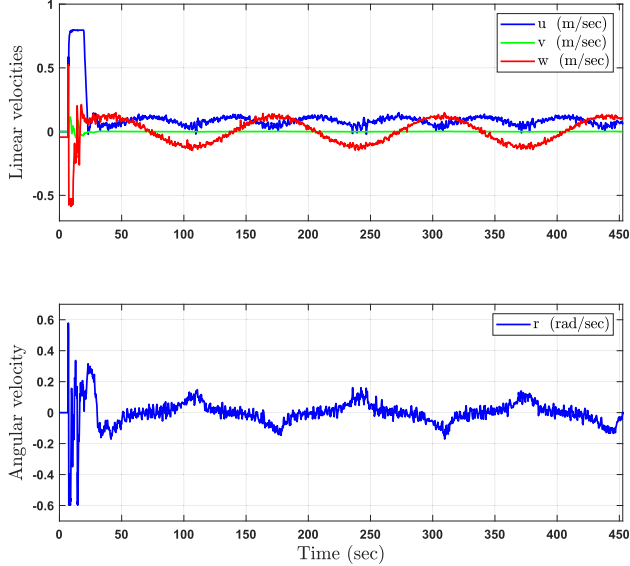


Fig. 10. Obstacle-free scenario: the evolution of the vehicle velocities during the task operation.

[39], a realistic simulation environment developed in the robot operating system (ROS) [40] framework with 1-ms time step, which is common in a real-time operation with an underwater robotic system. The constrained NMPC employed in this work is implemented using the NLOpt Optimization library [41].

We conducted an underwater inspection task under external disturbances representing ocean currents and waves. More specifically, two separate scenarios have been considered: 1) obstacle free and 2) constrained workspace, including obstacles. In particular, obstacle-free scenario consists of a pipeline inspection task where the tracking control problem for an underactuated AUV was considered in along a pipeline structure, while, in the constrained scenario, the tracking control problem was considered in a workspace, including two obstacles, where their locations in the  $xy$  plane are given by

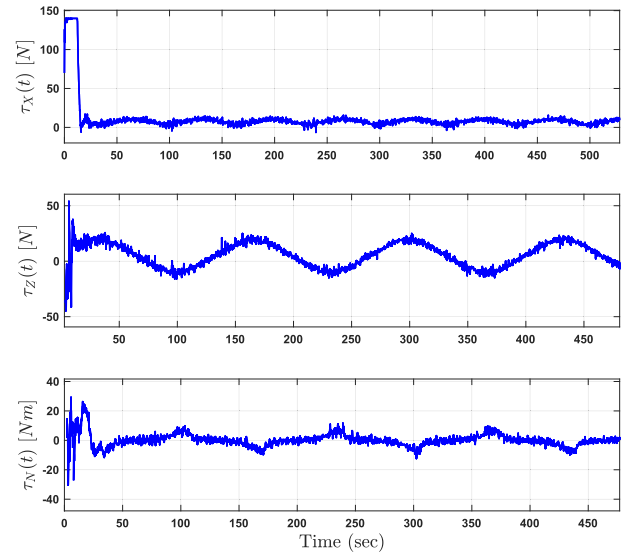


Fig. 11. Obstacle-free scenario: the control input signals during the task operation.

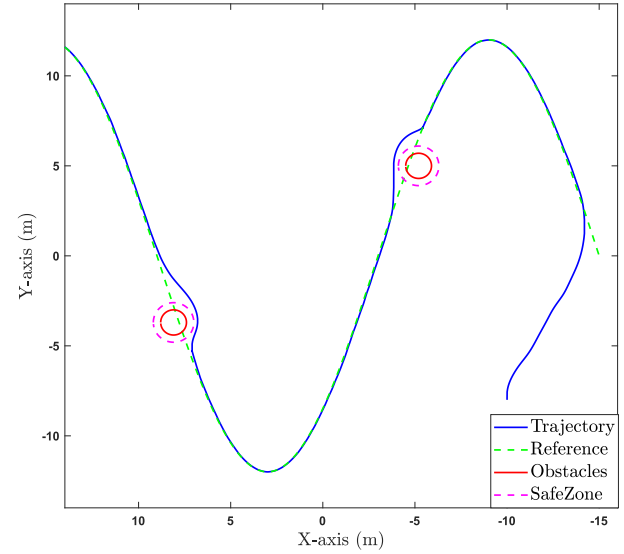


Fig. 12. Constrained scenario: the evolution of the vehicle and desired trajectory in the horizontal plane.

$\mathbf{p}_1 = [-5, 5]^\top$  and  $\mathbf{p}_2 = [7.8, -4]^\top$ , respectively (see Fig. 6).

In both scenarios, we considered a unicycle-like underactuated AUV where its dynamic parameters are given in Table I. The capability sensing range and the horizon of the FHOCP are considered as  $\bar{R} = 3$  and  $N = 10 * t = 1.0$  s, respectively. Moreover, the predefined upper bound of the vehicle velocities in (7) is defined as  $\bar{u} = 0.8$  (m/s),  $\bar{v} = 0.04$  (m/s),  $\bar{w} = 0.6$  (m/s), and  $\bar{r} = 0.6$  (rad/s). Furthermore, each of the three control inputs must obey the following input constraint:  $\bar{\tau}_X = 140$  N,  $\bar{\tau}_Z = 100$  N, and  $\bar{\tau}_N = 60$  Nm. The control design parameters were chosen as  $k = 1.0$ ,  $\varpi = 4.0$ , and  $k = 5.0$ . In both scenarios, the vehicle initially was at rest and was request to track a desired trajectory within the workspace. In addition, in the subsequent simulation study, the dynamics

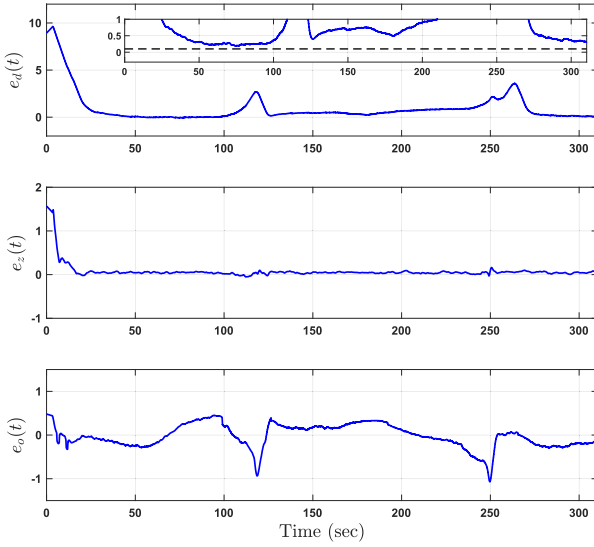


Fig. 13. Constrained scenario: the evolution of the transformed errors.

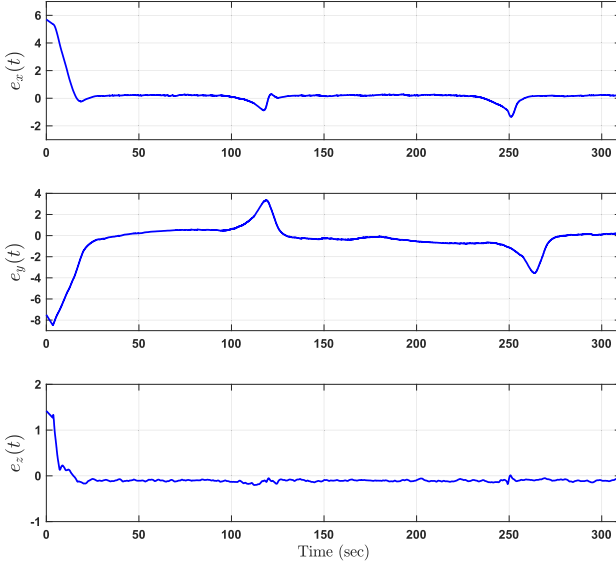


Fig. 14. Constrained scenario: the evolution of the real errors.

of the considered AUV were affected by external disturbances in the form of slowly time varying sea currents acting along  $X$ -,  $Y$ -,  $Z$ -, and  $N$ -axes of the vehicle frame modeled by the corresponding dynamics  $\delta_X = 0.2 \sin(2(\pi/15)t)$  (m/s),  $\delta_Y = 0.2 \sin(2(\pi/15)t)$  (m/s)  $\delta_Z = 0.2 \cos(2(\pi/15)t)$  (m/s), and  $\delta_N = 0.2 \sin(2(\pi/15)t)$  (m/s) (i.e., we set  $\bar{\delta} = 0.6$  and  $\bar{\delta}_Y = 0.2$ ). Furthermore, we considered 20% uncertainties on the AUV dynamic parameters (i.e., we set  $\bar{y} = 0.2$ ).

#### A. Obstacle-Free Scenario

The vehicle initially was at rest from the location  $\eta(0) = [-15, -12, 10, 0]$  and was requested to track a trajectory along a pipeline structure. The desired trajectory involving line and curved segments was defined by  $p_d(t) = [-10 + 0.015 * \pi t, 2.5 \sin(0.015\pi t), 6 \cos(0.015\pi t)]^\top$ . The results are given in Figs. 7–11, respectively. The trajectory of the

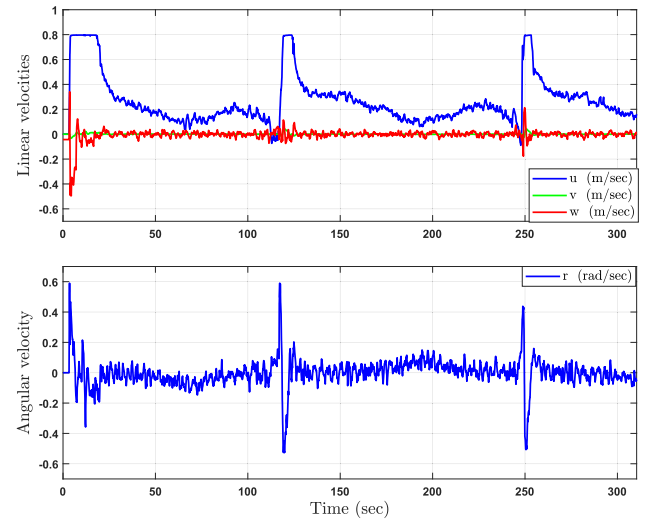


Fig. 15. Constrained scenario: the evolution of the vehicle velocities during the task operation.

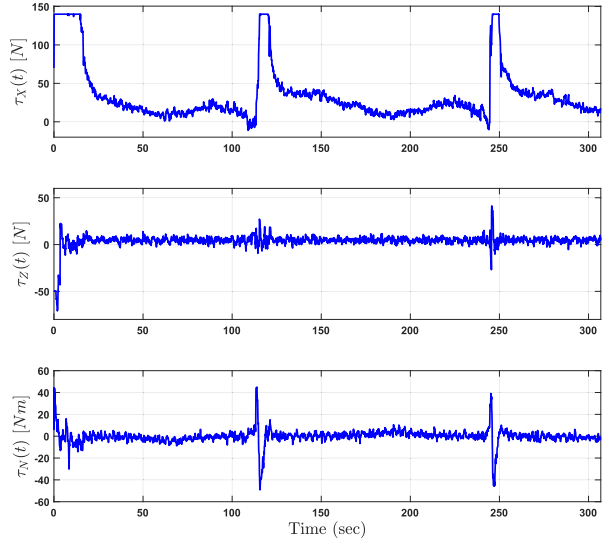


Fig. 16. Constrained scenario: the control input signals during the task operation.

system within the workspace is depicted in Fig. 6 and in 3-D space in Fig. 7, respectively. It can be seen that the vehicle performs successfully the trajectory tracking task along the pipeline structure. The evolution of the transformed and real error coordinates is shown in Figs. 8 and 9, respectively. It can be seen that the real errors remain close to zero, and the constraint  $e_d(t) \geq \epsilon$ ,  $\epsilon = 0.1$  of (19) remain satisfied during the task operation.

#### B. Constrained Scenario

The vehicle initially was at rest from the location  $\eta(0) = [-10, -8, 9, 0]$  and was request to track a trajectory along the pipeline structure. The desired trajectory involving line and curved segments was defined by  $p_d(t) = [-15 + 0.1 t, 12 \sin((\pi/120)t), 8]^\top$ . Notice that the desired trajectory that is required to be tracked by the AUV coincides with

obstacles positions. The obstacles are modeled according to the spherical world representations as consecutive spheres (i.e., cylinders) with radius  $r_{\pi_i} = 0.7$  m,  $i = \{1, \dots, 2\}$ . The radius of the sphere  $\mathcal{B}(\eta_1, \tilde{r})$  that covers all the vehicle volume (i.e., main body and additional equipment) is defined as  $\tilde{r} = 0.4$ . However, for the clarity of presentation, we depict it as a safe zone around the obstacles where the vehicle center  $\eta_1$  (denoted by blue line in Fig. 12) should not violate it.

The capability sensing range and the horizon of the FHOCP are considered as  $\bar{R} = 3$  and  $N = 10 * t = 1.0$  s, respectively, satisfying the condition (41). Notice that the obstacles are detected and considered by the controller when they are within the sensing range of the robot. Finally, the parameters  $\epsilon_d$  and  $\epsilon_r$  defined in (19) are set to  $\epsilon_d = 0.1$  and  $\epsilon_r = 0.1$ .

The simulation scenario has been conducted in such a way that the robot is required to track the desired trajectory, which coincides two times with obstacles. The results are given in Figs. 12–16. The trajectory of the system within the workspace is depicted in Fig. 6 and along the horizontal plane in Fig. 12. It can be seen that the vehicle performs, successfully, the trajectory tracking while safely avoids the obstacles within the workspace. We observe that the robot has been left the desired trajectory when it was needed in order to avoid the obstacles. The evolution of the transformed and real error coordinates is shown in Figs. 13 and 14, respectively. It can be seen that the real errors remain close to zero, and the constraints  $e_d(t) \geq \epsilon$ ,  $\epsilon = 0.1$  of (19) remain satisfied during the task operation. In Fig. 15, the vehicle velocities are presented, and the respective constraints are satisfied. Finally, in Fig. 16, the vehicle's thruster inputs are shown. As can be seen, the input constraints are also satisfied.

*Video:* A video demonstrating the simulation scenarios of this section can be found in the following link: <https://youtu.be/v-rWqNsCfY0>

## VI. CONCLUSION

This article presents a robust trajectory tracking control for underactuated AUVs operating in a constrained workspace, including obstacles. The purpose of the controller is to steer the underactuated AUV on a desired trajectory inside a constrained and dynamic workspace. The workspace knowledge (i.e., obstacles' locations) is constantly updated online via the vehicle's sensors. Obstacle avoidance with any of the detected obstacles is guaranteed, despite the presence of external disturbances. Moreover, various constraints such as obstacles, workspace boundaries, and predefined upper bound of the vehicle velocity (requirements for various underwater tasks, such as seabed inspection and mosaicking) are considered during the control design. The proposed feedback control law consists of two parts: 1) an FHOCP and 2) a state feedback law that is tuned off-line and guarantees that the real trajectories remain inside a tube centered along the nominal trajectories. The closed-loop system has analytically guaranteed stability and convergence properties. Future research efforts will be devoted toward extending the proposed methodology for multiple AUVs operating in a dynamic environment, including not only static but also moving obstacles.

## REFERENCES

- [1] J. Yuh, "Design and control of autonomous underwater robots: A survey," *Auton. Robots*, vol. 8, no. 1, pp. 7–24, 2000.
- [2] X. Xiang, L. Lapierre, and B. Jouvencel, "Smooth transition of AUV motion control: From fully-actuated to under-actuated configuration," *Robot. Auto. Syst.*, vol. 67, pp. 14–22, May 2015.
- [3] N. Wang, H. R. Karimi, H. Li, and S.-F. Su, "Accurate trajectory tracking of disturbed surface vehicles: A finite-time control approach," *IEEE/ASME Trans. Mechatronics*, vol. 24, no. 3, pp. 1064–1074, Jun. 2019.
- [4] T. Fossen, *Handbook of Marine Craft Hydrodynamics and Motion Control*. Hoboken, NJ, USA: Wiley, 2011.
- [5] C. Paliotta, E. Lefeber, K. Y. Pettersen, J. Pinto, M. Costa, and J. T. de Figueiredo Borges de Sousa, "Trajectory tracking and path following for underactuated marine vehicles," *IEEE Trans. Control Syst. Technol.*, vol. 27, no. 4, pp. 1423–1437, Jul. 2019.
- [6] Y. Li, C. Wei, Q. Wu, P. Chen, Y. Jiang, and Y. Li, "Study of 3 dimension trajectory tracking of underactuated autonomous underwater vehicle," *Ocean Eng.*, vol. 105, pp. 270–274, Sep. 2015.
- [7] A. P. Aguiar and A. M. Pascoal, "Dynamic positioning and way-point tracking of underactuated AUVs in the presence of ocean currents," *Int. J. Control.*, vol. 80, no. 7, pp. 1092–1108, Jul. 2007.
- [8] J. Guerrero, J. Torres, V. Creuze, and A. Chemori, "Trajectory tracking for autonomous underwater vehicle: An adaptive approach," *Ocean Eng.*, vol. 172, pp. 511–522, Jan. 2019.
- [9] L. Lapierre and B. Jouvencel, "Robust nonlinear path-following control of an AUV," *IEEE J. Ocean. Eng.*, vol. 33, no. 2, pp. 89–102, Apr. 2008.
- [10] B. Qiu, G. Wang, Y. Fan, D. Mu, and X. Sun, "Adaptive sliding mode trajectory tracking control for unmanned surface vehicle with modeling uncertainties and input saturation," *Appl. Sci.*, vol. 9, no. 6, p. 1240, Mar. 2019.
- [11] Z. Yan, M. Wang, and J. Xu, "Robust adaptive sliding mode control of underactuated autonomous underwater vehicles with uncertain dynamics," *Ocean Eng.*, vol. 173, pp. 802–809, Feb. 2019.
- [12] T. Elmokadem, M. Zribi, and K. Youcef-Toumi, "Trajectory tracking sliding mode control of underactuated AUVs," *Nonlinear Dyn.*, vol. 84, no. 2, pp. 1079–1091, Apr. 2016.
- [13] L. Qiao and W. Zhang, "Double-loop integral terminal sliding mode tracking control for UUVs with adaptive dynamic compensation of uncertainties and disturbances," *IEEE J. Ocean. Eng.*, vol. 44, no. 1, pp. 29–53, Jan. 2019.
- [14] N. Wang and M. Joo, "Self-constructing adaptive robust fuzzy neural tracking control of surface vehicles with uncertainties and unknown disturbances," *IEEE Trans. Control Syst. Technol.*, vol. 23, no. 3, pp. 991–1002, May 2015.
- [15] M. Carreras, J. Yuh, J. Batlle, and P. Ridao, "A behavior-based scheme using reinforcement learning for autonomous underwater vehicles," *IEEE J. Ocean. Eng.*, vol. 30, no. 2, pp. 416–427, Apr. 2005.
- [16] B. S. Park, "Neural network-based tracking control of underactuated autonomous underwater vehicles with model uncertainties," *J. Dyn. Syst., Meas., Control*, vol. 137, no. 2, Feb. 2015.
- [17] B. M. Patre, P. S. Londhe, L. M. Waghmare, and S. Mohan, "Disturbance estimator based non-singular fast fuzzy terminal sliding mode control of an autonomous underwater vehicle," *Ocean Eng.*, vol. 159, pp. 372–387, Jul. 2018.
- [18] B. Sun, D. Zhu, and S. X. Yang, "An optimized fuzzy control algorithm for three-dimensional AUV path planning," *Int. J. Fuzzy Syst.*, vol. 20, no. 2, pp. 597–610, Feb. 2018.
- [19] C. P. Bechlioulis, G. C. Karras, S. Heshmati-Alamdari, and K. J. Kyriakopoulos, "Trajectory tracking with prescribed performance for underactuated underwater vehicles under model uncertainties and external disturbances," *IEEE Trans. Control Syst. Technol.*, vol. 25, no. 2, pp. 429–440, Mar. 2017.
- [20] S. Heshmati-Alamdari, G. C. Karras, P. Marantos, and K. J. Kyriakopoulos, "A robust predictive control approach for underwater robotic vehicles," *IEEE Trans. Control Syst. Technol.*, early access, Oct. 2019, doi: [10.1109/TCST.2019.2939248](https://doi.org/10.1109/TCST.2019.2939248).
- [21] F. Allgöwer, R. Findeisen, and Z. K. Nagy, "Nonlinear model predictive control: From theory to application," *J.-Chin. Inst. Chem. Eng.*, vol. 35, no. 3, pp. 299–315, 2004.
- [22] C. Shen, Y. Shi, and B. Buckingham, "Trajectory tracking control of an autonomous underwater vehicle using Lyapunov-based model predictive control," *IEEE Trans. Ind. Electron.*, vol. 65, no. 7, pp. 5796–5805, Jul. 2018.

- [23] C. V. Caldwell, D. D. Dunlap, and E. G. Collins, "Motion planning for an autonomous underwater vehicle via sampling based model predictive control," in *Proc. Oceans MTS/IEEE Seattle*, Sep. 2010, pp. 1–6.
- [24] L. V. Steenson *et al.*, "Model predictive control of a hybrid autonomous underwater vehicle with experimental verification," *Proc. Inst. Mech. Eng., M, J. Eng. Maritime Environ.*, vol. 228, no. 2, pp. 166–179, 2014.
- [25] C. Shen, B. Buckham, and Y. Shi, "Modified C/GMRES algorithm for fast nonlinear model predictive tracking control of AUVs," *IEEE Trans. Control Syst. Technol.*, vol. 25, no. 5, pp. 1896–1904, Sep. 2017.
- [26] C. Petres, Y. Pailhas, P. Patron, Y. Petillot, J. Evans, and D. Lane, "Path planning for autonomous underwater vehicles," *IEEE Trans. Robot.*, vol. 23, no. 2, pp. 331–341, Apr. 2007.
- [27] D. N. Subramani and P. F. J. Lermissiaux, "Energy-optimal path planning by stochastic dynamically orthogonal level-set optimization," *Ocean Model.*, vol. 100, pp. 57–77, Apr. 2016.
- [28] H. K. Khalil, *Nonlinear Systems*. Upper Saddle River, NJ, USA: Prentice-Hall, 2002.
- [29] G. C. Karras, S. G. Loizou, and K. J. Kyriakopoulos, "Towards semi-autonomous operation of under-actuated underwater vehicles: Sensor fusion, on-line identification and visual servo control," *Auto. Robots*, vol. 31, no. 1, pp. 67–86, Jul. 2011.
- [30] T. Fossen, *Guidance and Control of Ocean Vehicles*. New York, NY, USA: Wiley, 1994.
- [31] D. E. Koditschek and E. Rimon, "Robot navigation functions on manifolds with boundary," *Adv. Appl. Math.*, vol. 11, no. 4, pp. 412–442, Dec. 1990.
- [32] H. Michalska and D. Q. Mayne, "Robust receding horizon control of constrained nonlinear systems," *IEEE Trans. Autom. Control*, vol. 38, no. 11, pp. 1623–1633, Nov. 1993.
- [33] H. Chen and F. Allgöwer, "A quasi-infinite horizon nonlinear model predictive control scheme with guaranteed stability," *Automatica*, vol. 34, no. 10, pp. 1205–1217, 1998.
- [34] D. Q. Mayne, J. B. Rawlings, C. V. Rao, and P. O. M. Scokaert, "Constrained model predictive control: Stability and optimality," *Automatica*, vol. 36, no. 6, pp. 789–814, Jun. 2000.
- [35] L. Grüne and J. Pannek, *Nonlinear Model Predictive Control: Theory and Algorithms* (Communications and Control Engineering). London, U.K.: Springer-Verlag, 2011, doi: [10.1007/978-0-85729-501-9](https://doi.org/10.1007/978-0-85729-501-9).
- [36] S. Yu, C. Maier, H. Chen, and F. Allgöwer, "Tube MPC scheme based on robust control invariant set with application to Lipschitz nonlinear systems," *Syst. Control Lett.*, vol. 62, no. 2, pp. 194–200, Feb. 2013.
- [37] A. Nikou and D. V. Dimarogonas, "Decentralized tube-based model predictive control of uncertain nonlinear multiagent systems," *Int. J. Robust Nonlinear Control*, vol. 29, no. 10, pp. 2799–2818, Jul. 2019.
- [38] S. Yu, C. Maier, H. Chen, and F. Allgöwer, "Tube MPC scheme based on robust control invariant set with application to lipschitz nonlinear systems," *Syst. Control Lett.*, vol. 62, no. 2, pp. 194–200, Feb. 2013.
- [39] M. Prats, J. Perez, J. J. Fernandez, and P. J. Sanz, "An open source tool for simulation and supervision of underwater intervention missions," in *Proc. IEEE/RSJ Int. Conf. Intell. Robots Syst.*, Oct. 2012, pp. 2577–2582.
- [40] M. Quigley *et al.*, "Ros: An open-source robot operating system," in *Proc. ICRA Workshop Open Source Softw.*, 2009, pp. 1–5.
- [41] S. G. Johnson. *The NLOpt Nonlinear-Optimization Package*. Accessed: Jun. 21, 2020. [Online]. Available: <http://ab-initio.mit.edu/wiki/index.php/nlopt>



**Shahab Heshmati-Alamdar** received the Diploma degree in mechanical engineering, the master's degree in robotics and automatic control, and the Ph.D. degree in mechanical engineering from the National Technical University of Athens (NTUA), Athens, Greece, in 2009, 2012, and 2018, respectively.

He is currently a Post-Doctoral Researcher with the Division of Decision and Control Systems, School of Electrical Engineering and Computer Science, KTH Royal Institute of Technology, Stockholm, Sweden. His research interests include navigation and sensor-based motion planning of unmanned autonomous vehicles (aerial, ground, and underwater), reinforcement learning, task planning, and distributed control of multirobot systems, such as free-flying manipulators and autonomous robotic vehicles.



**Alexandros Nikou** received the Diploma degree in electrical and computer engineering and the M.Sc. degree in automatic control both from the National Technical University of Athens (NTUA), Athens, Greece, in 2012 and 2014, respectively, and the Ph.D. degree in electrical engineering and computer science from the KTH Royal Institute of Technology, Stockholm, Sweden, in 2019.

He is currently a Senior Researcher with Ericsson Research AI, Stockholm. His current research interests include distributed reinforcement learning and formal methods.



**Dimos V. Dimarogonas** (Senior Member, IEEE) was born in Athens, Greece, in 1978. He received the Diploma degree in electrical and computer engineering and the Ph.D. degree in mechanical engineering from the National Technical University of Athens (NTUA), Athens, in 2001 and 2007, respectively.

He has held post-doctoral positions at the KTH Royal Institute of Technology, Stockholm, Sweden, and the Massachusetts Institute of Technology (MIT), Cambridge, MA, USA. He is currently a Professor with the Division of Decision and Control, KTH Royal Institute of Technology. His current research interests include multiagent systems, hybrid systems and control, robot navigation, and networked control.

Dr. Dimarogonas serves on the Editorial Board of *Automatica* and the IEEE TRANSACTIONS ON CONTROL OF NETWORK SYSTEMS.